Coordination polymers nanoparticles for bioimaging

Salvio Suárez-García,[a] Rubén Solórzano,[a,b] Fernando Novio,[a,b] Ramon Alibés,[b] Félix Busqué,[b] Daniel Ruiz-Molina[a]*

[a]*Catalan Institute of Nanoscience and Nanotechnology (ICN2), CSIC and BIST, Campus UAB, Bellaterra, 08193 Barcelona, Spain.*

[b]*Departament de Química, Universitat Autònoma de Barcelona (UAB), Campus UAB, Cerdanyola del Vallès 08193, Barcelona, Spain*

*Corresponding author: e-mail: dani.ruiz@icn2.cat (D.R.-M.)

Abstract.

Early diagnosis of patient diseases is subjected to the appropriate use of bioimaging techniques. For this reason, the development of contrast agents that improve and enhance the response of current clinical imaging practices is a pressing concern. Non-invasive bioimaging techniques most often need specific probes to follow and measure biological routes in living systems. These molecular imaging agents must exhibit: I) a remarkable contrast effect, i.e. a high signal-to-noise ratio under real physiological conditions, II) pronounced *in vivo* stability under the effect of numerous enzymes or proteases present in serum or targeted tissue equilibrated with a fast clearance from healthy organs and III) low cost and eco-friendly production. To overcome current drawbacks that hindrance the full development of the different bioimaging techniques, several groups are exploring nanoparticles as contrast agents. In this scenario, coordination polymer nanoparticles have emerged as a handy platform offering predesigned unique advantages thanks to their chemical flexibility, structural diversity and tailoring skills. Indeed, these systems reveal high metal cargos, low toxicity and multifunctional character by adequately selecting the combination of metal ions and ligands. Moreover, in a reminiscent way of organic polymeric nanoparticles, coordination polymer nanoparticles have also demonstrated its ability to encapsulate therapeutic-active molecules, thus combining diagnostic and therapeutic functionalities, the so-called Theranostic nanomedicine. For all this reason the use of this family of nanoparticles as imaging contrast agents has attracted broad interest over the last years with numerous examples being reported. Herein we review main accomplishments in the area grouped according to the used technology, including magnetic resonance imaging, computed tomography, optical imaging, radioimaging or photoacoustic imaging.

Keywords: bioimaging, contrast agent, nanoparticle, coordination polymer, theranostic

Contents

Abbreviations: NP, nanoparticle; EPR, enhanced permeability and retention effect; CP, coordination polymer; NMOF, nanoscale metal-organic framework; CPN, coordination polymer nanoparticle; TEM, transmission electron microscopy; SEM, scanning electron microscopy; AZT, azidothymidine; MRI, magnetic resonance imaging; OI, optical imaging; RI, radioimaging; T_1*, longitudinal relaxivity;* T_2*, transversal relaxivity; CA, contrast agent; ROI, region-of-interest;* r_1*, longitudinal relaxation value;* r_2*, transversal relaxation value;* T_{1w}*,* T_1 *weighted imaging contrast;* T_{2w}*,* T_2 *weighted imaging contrast; SPION, superparamagnetic iron oxide nanoparticle; DOX, Doxorubicin; hD, hydrodynamic diameter; PEO, poly(ethylene-oxide); PEG, polyethylene glycol; DLS, dynamic light scattering; AA, anisamide; NIR, near-infrared; PDA, polydopamine; i.v., intravenous; Ce6, chlorine e6; PDT, photodynamic therapy; DHBC, double-hydrophilic block copolymer); DMCA, dual-mode contrast agent; CT, computed tomography; QD, quantum dot; AIE, aggregation-induced emission enhancement; Cur, curcuminoid; ANF, 6–amino fluorescein; CLSM, confocal laser scanning microscopy; rhod, rhodamine; GMP, gemcitabine monophosphate; FITC, fluorescein isothiocyanate; PET, positron emission tomography; SPECT, single photon emission computed–tomography; PAI, photoacoustic imaging; PVP, polyvinylpyrrolidone.*

1. INTRODUCTION

Timely diagnosis of diseases is central to apply early treatments and therefore, to increase the survival rate of patients. For this reason, the continuous development of more sophisticated approaches that improve the sensitivity and accuracy of medical imaging practices is an area of constant investigation. Research on molecular-based bioimaging probes to increase contrast at specific regions is one of such field of study. With this aim, bioimaging probes such as gadolinium or radiotracers metal complexes have been successfully used though they still raise many doubts about its biocompatibility and side effects. On top of that, the efficiency of discrete molecules can be compromised by non-specific distributions and rapid clearance. In this scenario, Nanotechnology brings new exciting opportunities for the design and development of functional systems with outstanding features for their application in bioimaging [1]. Nanoparticles (NPs) can be easily functionalised to improve the biodistribution and targeting, while can exhibit a multimodal imaging therapy [2]. Moreover, in the case of tumours, NPs exhibit enhanced preferential gathering thanks to the permeability and retention (EPR) effect [3].

To date, diverse families of NPs have been used as imaging agents, among them, organic NPs such as liposomes [4,5], micelles [6], carbon nanotubes[7], nanographene oxide [8] or inorganic materials [9,10,11] such as quantum dots [12], silica NPs [13], 2D transition metal dichalcogenide nanosheets [14], upconversion nanocomposites [15] or gold NPs [16]. During the last years, semiconducting polymer NPs, which are made of π-conjugated semiconducting polymers, have emerged as one of the most skilful organic agents for bioimaging. Their advantages are mainly due to their versatile light-responsive properties to meet the specific requirements for different bioimaging applications, ranging from molecular imaging to photothermal bioactivation and cancer phototherapy [17,18,19].

However, even though successful, most of these systems still need to improve diagnostic accuracy and their biosafety. This concern is especially relevant for inorganic and non-biodegradable NPs that accumulate in liver and spleen, resulting in latent long-term toxicity issues [20]. Failure targeting, harmful accumulations in organs, high immune response or non-optimised signals are other significant problems that can also hamper their use for future clinical translation. Consequently, the fabrication of a new generation of multifunctional NPs with adequate size and biodegradability profiles,

enhanced targeting, reduced accumulation in reticuloendothelial organs and rapid body clearance, represents a significant challenge nowadays.

Coordination polymers (CPs) are being studied for decades thanks to their synthetic flexibility, where a predesigned mixture of metal ions and organic ligands guarantees control over the chemical topology. The exquisite control and selection of constituent units allows for the formation of functional polymers with tuneable properties (e.g. porosity) [21]. However, the implementation of CPs in Medicine has traditionally remained elusive, mainly due to limitations in their administration and pharmacokinetics. Advances accomplished over the last years on the miniaturisation of CPs down to the nanometre scale have represented a novel opportunity for these materials in the field of Medicine, by offering improved colloidal dispersions, increased surface areas and optimised responses [22].

Nanoscale metal-organic frameworks, referred from now on as NMOFs, represent one of these families. NMOFs are crystalline porous coordination polymer nanostructures exhibiting large voids with high loading capacity and control over the cargo release. The crystalline character of NMOFs entails a systematic analysis of host-guest interactions and release studies, complemented by theoretical models. Consequently, these nanomaterials have raised considerable interest, and comprehensive reviews summarising progress in NMOFs are available [23,24]. Another family of CPs attracting attention during the last years is that of amorphous coordination polymer NPs (CPNs) [25], also called nanoscale coordination polymers [26], infinite coordination polymers [27] or coordination polymer particles [28]. Even though these NPs are not mainly characterised by being highly porous systems, they can encapsulate several drugs with excellent yields, have excellent colloidal stabilities and show multifunctional properties that make them very attractive for their application in bioimaging. This capability is due to the fact that CPNs can incorporate active elements into their structure or entrap ready-to-use drugs (e.g. Doxorubicin, DOX) that can be released by the natural degradation of NPs or by external stimuli such as pH, light and enzymes, among others. Moreover, multifunctional systems are achieved by the functionalisation or incorporation of active probes (e.g. dyes) or metals (e.g. Fe) suitable for performing imaging. In this review, we will enlighten first the synthesis and characterisation of this innovative family of NPs to, later on, summarise in more detail the numerous examples so far reported for their use in the different bioimaging techniques drafted in **Figure 1**.

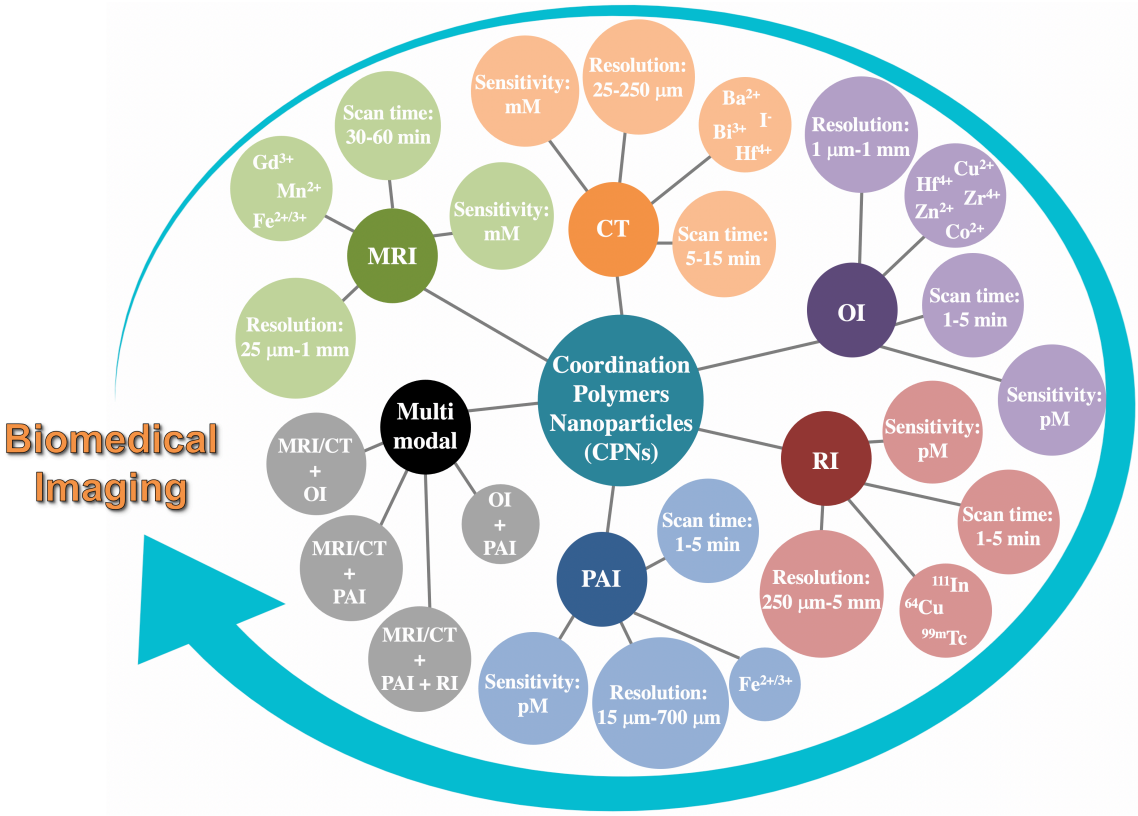

Figure 1. The use of coordination polymer nanoparticles (CPNs) in different bioimaging techniques reported in this review.

2. COORDINATION POLYMER NANOPARTICLES

Since first reported in 2005 by Mirkin [29] and Wang [30], the number of publications related to CPNs is growing exponentially. For their synthesis, metal ions and organic ligands are usually mixed in the presence of an antisolvent, a secondary solvent (e.g. water) that induces fast precipitation due to the insolubility of the final product (**Figure 2a**) [31]. The use of such out-of-equilibrium conditions leads to the formation of amorphous nanomaterials with spherical morphology that diminishes the interfacial free energy of the CPNs. Moreover, the dimensions can be tunned from few to hundred nanometres in size by controlling some parameters such as the rate of solvent addition (antisolvent) to the reaction mixture and/or the stirring speed [32]. As a representative, **Figure 2b** shows a CPN system ranging different sizes depending on the stirring speed. In this case, the increase of the agitation rate allowed for the formation of smaller NPs.

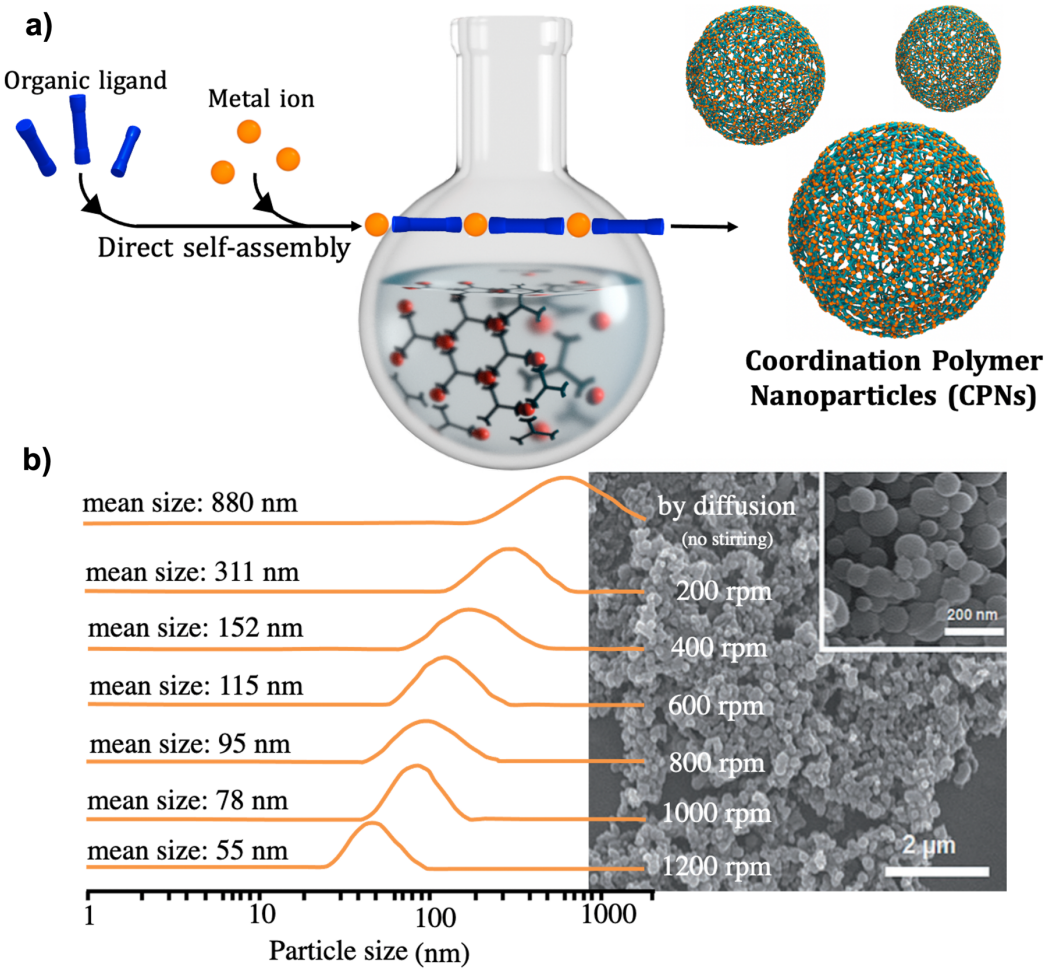

Figure 2. (a) Schematic synthetic methodology followed for the formation of CPNs using out-of-equilibrium conditions. (b) Representative scanning electron microscopy (SEM) image of the resulting NPs with fine-tuned modification of the diameter with the stirring rate. Reproduced from ref. [31] and [32].

Besides fast precipitation, other approaches to obtain CPNs have also been used [33], including dip-pen nanolithography [34,35], reverse micro-emulsions [36] or lab-on-a-chip implementation [37]. Scientists have also made efforts to understand their mechanism formation [38], to tune their structure and composition [39,40] or the conversion through the exchange of metals and/or organic ligands [41,42]. However, one of the most relevant challenges that scientists are facing is to control their surface functionality [43,44]. For instance, incorporation of terminal carboxylic groups in one of the ligands allowed Novio *et al.* to report NPs with boosted thermal and colloidal stabilities. Moreover, carboxylic groups remaining on the surface of the NP were subsequently functionalised using peptide coupling reactions [45], allowing for the incorporation of other functional groups [46] or the construction of complex hybrid systems on surfaces [47].

As regards its application in biological environments, the high chemical flexibility of coordination chemistry has allowed the fabrication of pH-responsive NPs of relevance for the controlled drug release given the different acidity between intra- and extracellular environments [48,49,50,51,52,53,54,55,56,57,58,59,60]. For instance, Nador *et al*. demonstrated the differential pH-responsiveness of two structurally analogous bis(catechol)-based NPs containing either a pH-sensitive imine or non-sensitive alkyl ligands [61]. Besides pH [62,63,64,65], other potential stimuli for controlled cargo release might include redox [66,67], light-responsive [68,69,70] or multi stimuli-responsive systems [71,72,73,74,75,76,77]. Another validated relevant characteristic of CPNs is the encapsulation and controlled release of active pharmaceutical ingredients and other substances. For this, drugs can be incorporated as constitutive building blocks of the polymeric unit (chemical entrapment) or through the physical encapsulation within the CPNs [78]. Physical encapsulation of organic dyes, magnetic NPs, or luminescent quantum dots was already reported back in 2009 [79]. One year later, the same authors showed that these capsules not only can encapsulate but also can release active molecules as polymeric NPs do [80]. On the other side, chemical-guided encapsulation allows control of the release kinetics and better encapsulation yields as the drug release is not triggered by diffusion mechanisms but limited by the degradation of the NP. As a representative example, the use of active metal drugs, such as Pt-based molecules, as polymeric nodes of the coordination network, is one of the most used strategies [81]. Another example of chemical entrapment is the incorporation of drugs in the form of chelating ligands. In one of the few examples so far reported, Solórzano *et al*. recently described the use of CPNs as efficient carriers for AIDS/HIV therapy upon functionalisation with an anti-HIV drug (azidothymidine, AZT) chelated to catechol groups through a spacer, which is sensitive to enzymatic hydrolysis [82]. A schematic illustration of this approach is shown in **Figure 3**.

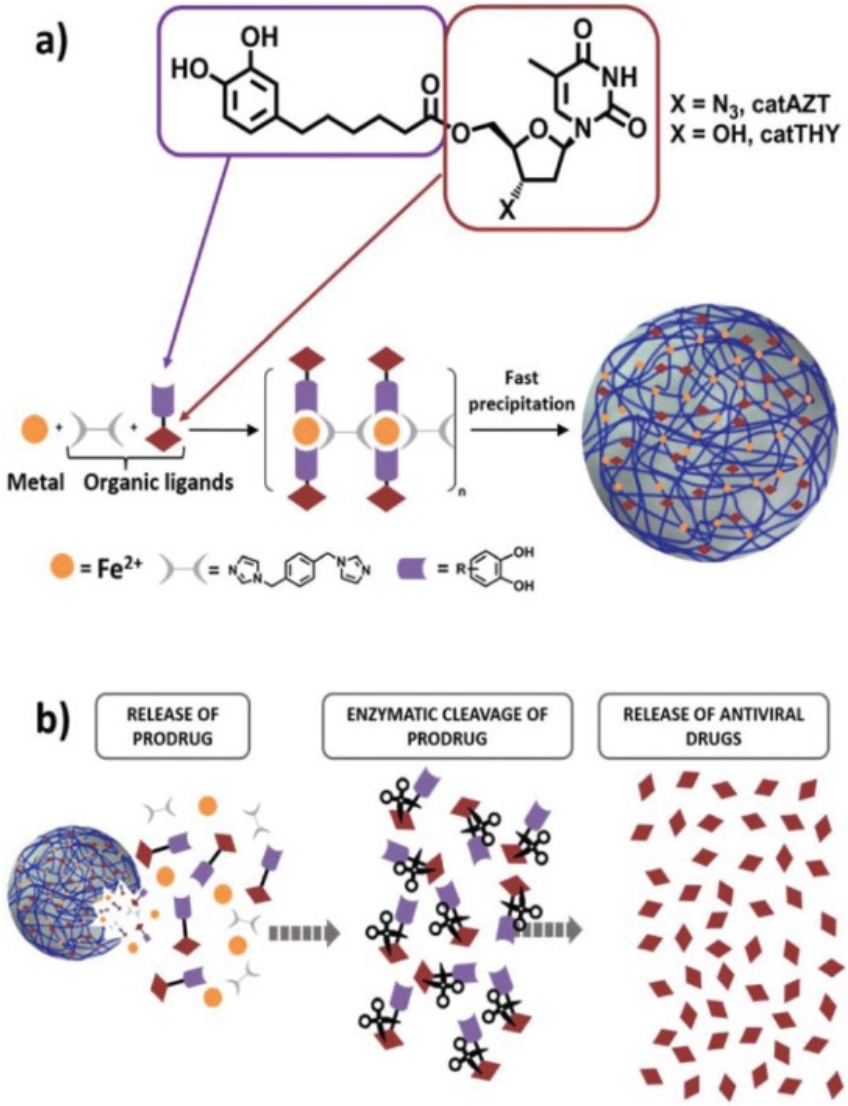

Figure 3. (a) Illustration of a catechol unit merged to the antiviral AZT drug by an enzymatically cleavable bond and the reaction of this ligand (catAZT or catTHY) with iron and a bis-imidazole to form nanoparticles (NPs). (b) Two-steps mechanism for the antiviral drug release from the NP constructs. First, the release of the catAZT ligand as a result of particle degradation and second enzymatic cleavage of AZT from the catechol derivative. Adapted with permission from ref. [82], Copyright 2019 Royal Society of Chemistry.

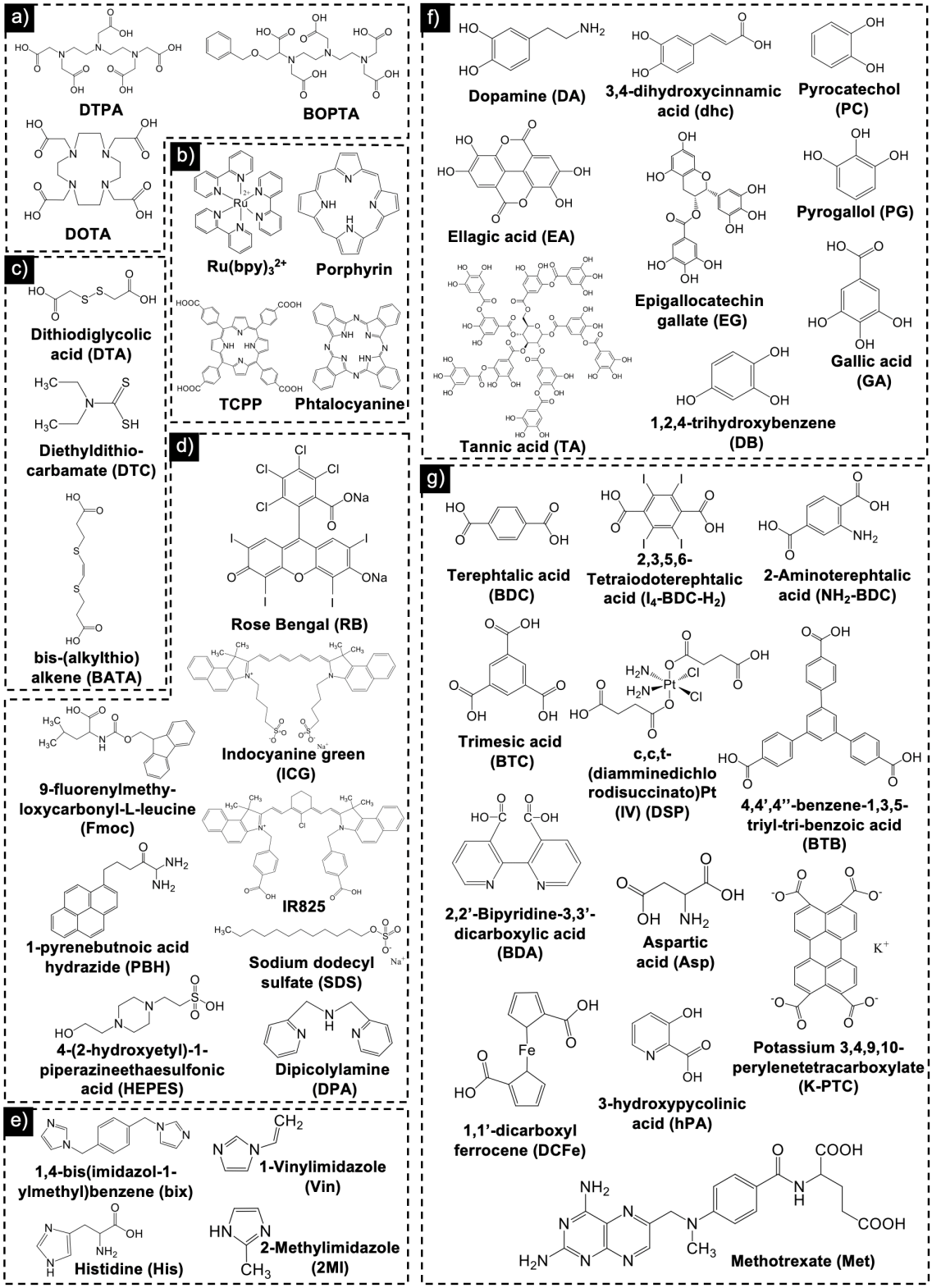

Scheme 1. Chemical structures used for the formation of CPNs. The most used ligands are classified in different groups: (a) chelating agents; (b) porphirin-like rings; (c) thiol-based; (d) optical-active; (e) imidazole-based; (f) catechol-based and (g) carboxylic-based ligands.

3. CPNs FOR BIOMEDICAL IMAGING

The study and development of innovative imaging probes based on CPNs as a novel family of NPs have raised an enormous interest in several imaging techniques, among them magnetic resonance imaging (MRI), optical imaging (OI) and radioimaging (RI). CPNs have reported several properties and advantages over other nanomaterials allowing to overcome some of the challenges in the diagnosis and monitoring of diseases. Moreover, the simultaneous incorporation of diagnostic and therapeutic functionalities within a single nanoplatform provides the desired multifunctional character, the so-called Theranostic nanomedicine [83]. The most relevant examples of CPNs for bioimaging are grouped and revised next.

3.1. Magnetic Resonance Imaging (MRI).

MRI is a broadly used technique that affords images of the patient with high spatial resolution. The non-invasive nature of MRI, together with the high increased depth penetration, makes this imaging technique the most clinically used nowadays. Its basis lies in the ability to detect the reorientations of the nuclear spin of hydrogen atoms (water proton-based ^{1}H-MRI). Three different parameters mainly influence the signal intensity detected by MRI equipment: I) the longitudinal (T_1) and transversal (T_2) relaxivity times, II) the cell environment and III) the proton density [84,85]. One of the main limitations of this radiation-free technique is the low sensitivity due to the low intrinsic contrast provided by the tissues. In order to overcome this limitation, the use of external contrast agents (CAs) is a need. A typical CA is able to improve image resolution and efficacy as it amends the relaxation times of protons in water molecules when a magnetic field is applied. Furthermore, administered CAs can be accumulated in specific areas, called Region-Of-Interest (ROI), thus improving the signal detected.

There exist mainly two types of CAs: positive ones, which reduce T_1 relaxation times and increases signal intensity (bright contrast), and negative ones, which predominantly shorten T_2 relaxation times providing reductions in signal intensity (dark contrast). Therefore, the performance of CAs is mostly evaluated by their longitudinal (r_1) and transversal (r_2) relaxation value ratios. Clinical T_1-CAs are mainly small molecules coming from the chelation of MRI-active metal ions, such as gadolinium complexes (Gd^{3+}), or manganese oxide (Mn^{2+}) that enhances the T_1-weighted contrast (T_{1w}). On the

other hand, T_2 CAs mainly involve superparamagnetic iron oxide compounds (SPIONs), showing darker contrast T_2-weighted images (T_{2w}). However, though successful, the r_1 and r_2 parameters offered by the current clinical CAs are modest, sometimes resulting still in ambiguous images after MRI analysis. These drawbacks cause the administration of high doses of CAs, generating risk for the health of the patients [86,87,88,89,90,91]. Aiming to improve the sensitivity while minimising the intrinsic toxicity and side effects of MRI CAs, efforts have been made to incorporate CAs into nanostructures that do not accumulate for a long term and have adequate clearance from the body [92,93]. For instance, Lin *et al*. reported mesoporous silica nanospheres coated with gadolinium complexes as highly efficient MRI CAs [94]. The incorporation of CAs in NMOFs has also been reported [95]. In the literature, the number of NPs described for MRI is extensive, here we will focus on the several successful examples of CPNs that have been so far reported, as presented next. For a better discussion and comparison between commercial CAs and reported CAs-based CPNs, the relaxivity parameters are summarised in **Table 1** and **2**, respectively.

Gadolinium

He *et al*. reported acid-degradable CPNs with a hydrodynamic diameter (hD) of 93.2 nm and enhanced *in vitro* T_1 signals by the reaction of Gd^{3+} ions and 2-amino-1,4-benzenedicarboxylic acid (NH_2-BDC) under solvothermal conditions [96]. The authors demonstrated that the CPNs become MRI-active at low pH due to their decomposition, facilitating the interaction with water molecules. In an acidic environment (pH = 5.5) the protonation of carboxyl groups present in the NH_2-BDC ligand induced the weakening of metal-ligand coordination inducing a pH-triggered decomposition of the NPs. At this pH, an r_1 value of 6.58 $mM^{-1}s^{-1}$was obtained, which was 39-fold higher than at pH = 7.4 (r_1 = 0.18 $mM^{-1}s^{-1}$). Furthermore, such pH-responsive-degradation system improves the biocompatibility, facilitates their clearance from the organism and last but not least, triggers the release of the encapsulated DOX molecules with therapeutic efficacy in targeted tumour cells. Other strategy for the rapid clearance of toxic gadolinium ions without compromising the imaging contrast is having control over the final dimensions of the CPNs. For instance NPs with diameters less than 8 nm can be excreted by the kidneys and reach the bladder easily [97] while increasing the exchange between Gd^{3+} and bulk water molecules thanks to its high surface-to-volume ratio. As an example, Perrier *et al*. reported cyano-bridged $Gd^{3+}/[Fe(CN)_6]^{3-}$ CPNs

showing 3-4 nm in diameter [98]. The resulting CPNs were synthesised by the stoichiometric mixture between $Gd(NO_3)_3 \cdot 6H_2O$ and $Na_3[Fe(CN)_6]$ in water and in the presence of D-mannitol as stabilising agent. The measured r_1 and r_2 relaxivities resulted in 11.4 and 12.6 $mM^{-1}s^{-1}$, respectively, using a 4.7 T MR scanner. The relaxivity values obtained were four times larger than those obtained for the commercial CA Gadoteridol under the same conditions (3.00 and 3.41 $mM^{-1}s^{-1}$ for r_1 and r_2, respectively) and the r_2/r_1 ratio was almost 1, which is a requirement for effective T_1 CA. Additional *in vivo* experiments demonstrated that the NPs stabilised with D-mannitol had a moderate long blood-circulation life-time while showing non-significant toxicity. Strategies to protect the CPNs by forming core-shell structures have also been described. In this sense, Ma *et al*. reported the coordination of Gd^{3+} with aspartic acid (Asp) and histidine (His) groups of an amphiphilic peptide present in the shell structure of self-assembled micelles containing poly(ethylene oxide) (PEO) [99]. The coordination with Gd^{3+} to form hybrid micelles was achieved by the addition of $GdCl_3 \cdot 6H_2O$ to a solution containing the performed micelles and under vigorous stirring. The resulting Gd-micelles showed a diameter size around 120 nm as provided by transmission electron microscopy (TEM). Under an external magnetic field (3T), the hybrid micelles showed r_1 = 34.12 $mM^{-1}s^{-1}$ and r_2 = 20.16 $mM^{-1}s^{-1}$ values, up to five times higher than those found for the commercial CA Magnevist® (Gd–diethylenetriamine pentacetic acid (DTPA), r_1 = 4.1 $mM^{-1}s^{-1}$ and r_2 = 4.6 $mM^{-1}s^{-1}$) tested under the same experimental conditions. Moreover, the hydrophobic core of micelles can accommodate anti-cancer drugs, such as DOX, that act as a therapeutic agent against tumour-bearing mice. Most recently in 2020, Qin *et al.* described the formation of metal-phenolic based CPs incorporating Gd^{3+} ions in the network [100]. The production of CPNs comprised two different steps. Firstly, tannic acid (TA), a polyphenol-based ligand, reacted with formaldehyde under alkaline conditions. This reaction induced the formation of TA-formaldehyde oligomer. In a second step, Gd^{3+} ions were added allowing for the trigger of oligomer assembly via metal-ligand coordination. TEM images showed the formation of spherical NPs with average diameter about 20.2 nm. In this case, polyvinylpyrrolidone (PVP) was added in order to prevent the formation of aggregates, avoiding fast precipitation of NPs. The validation of Gd-TA CPNs as MRI CAs exhibited high relaxivity parameters (r_1 = 25.5 $mM^{-1}s^{-1}$ and r_2 = 30.3 $mM^{-1}s^{-1}$) with r_2/r_1 ratio of 1.19. These results suggested this system as an excellent T_{1w} MRI. Interestingly, the same methodology could be applied for other MRI-active metals (e.g. Gd, Cu, Ni, Zn, Fe), thus demonstrating the high

versatility of polyphenol-based CPNs. Finally, the developed CPNs were validated *in vivo* through its intravenous (i.v.) injection in EMT-6 tumour-bearing mice. The results demonstrated an effective uptake of Gd-TA CPNs in the tumour with low short-term toxicity effects for the organism.

As previously described, successful examples of CPNs, which considerably reduce the dose of Gd^{3+} in comparison with commercial chelates, have been reported. This dose reduction has a beneficial impact by reducing toxicity without compromising the high CA response. Unfortunately, the progressive leach of free Gd^{3+} ions to the organism, which results in toxicity that limits their clinical applicability, is still unavoidable. The use of Gd^{3+} ions has different concerns. Briefly, some bio-metals, such as Zn and Cu, can be replaced by Gd^{3+}. Additionally, it has been reported the influence of Gd^{3+} in inducing the uptake in the extravascular space [101] and in the appearance of nephrogenic system fibrosis disease [102,103,104]. This toxicity problem becomes a higher risk in the long-term, mainly due to the accumulation of non-excreted metal. To address this issue, other active-MRI metals have been explored.

Manganese

Manganese, which has relaxivity values comparable to Gd, is one of the most used alternatives for the formation of NPs [105]. For instance, Taylor *et al*. described the controlled synthesis of CPNs, using Mn^{2+} and terephthalic (BTC)/trimesic (BTC) acids as coordination ligands, coated with a silica shell [94]. This strategy allowed for the synthesis of NPs by using a surfactant templated, base-catalysed condensation methodology. The coating conferred enough biostability and allowed for the additional functionalisation of the surface with a peptide (c(RGDfK)) that favour high *in vivo* r_1 values. Interestingly, the relaxivity parameters were measured under two different magnetic fields (3.0 and 9.4T), showing different values (r_1 of 28.8 $mM^{-1}s^{-1}$ (3T)/10.2 $mM^{-1}s^{-1}$ (9.4T) and r_2 of 65.5 $mM^{-1}s^{-1}$ (3T)/110.8 $mM^{-1}s^{-1}$ (9.4T)). In another work, Liu *et al*. reported CPNs by the microwave-assisted self-assembly of a Mn-bisphosphonate containing high loadings of zoledronate (63 ± 5 wt %) and Mn^{2+} ions (13 ± 4 wt %) in DMF/H_2O at 140 ºC for 10 min [106]. The resulting amorphous NPs, showed uniform shape with an hD of 55.8 nm as revealed by TEM. The system was further coated with: I) lipids and polyethylene glycol (PEG) to confer biocompatibility and improve their kinetics in biological environments and II) anisamide (AA) as an active targeting ligand to provide specific recognition to tumour cells (**Figure 4**). The *in*

vitro MRI studies highlighted the efficiency of the Mn-bisphosphonate CPN acting as a valid T_1 CA (r_1 = 7.6 $mM^{-1}s^{-1}$ and an r_2 = 70.3 $mM^{-1}s^{-1}$) and were tested with and without AA *in vitro* in MCF7 cells, showing enhanced signals in T_{1w} for the targeted system.

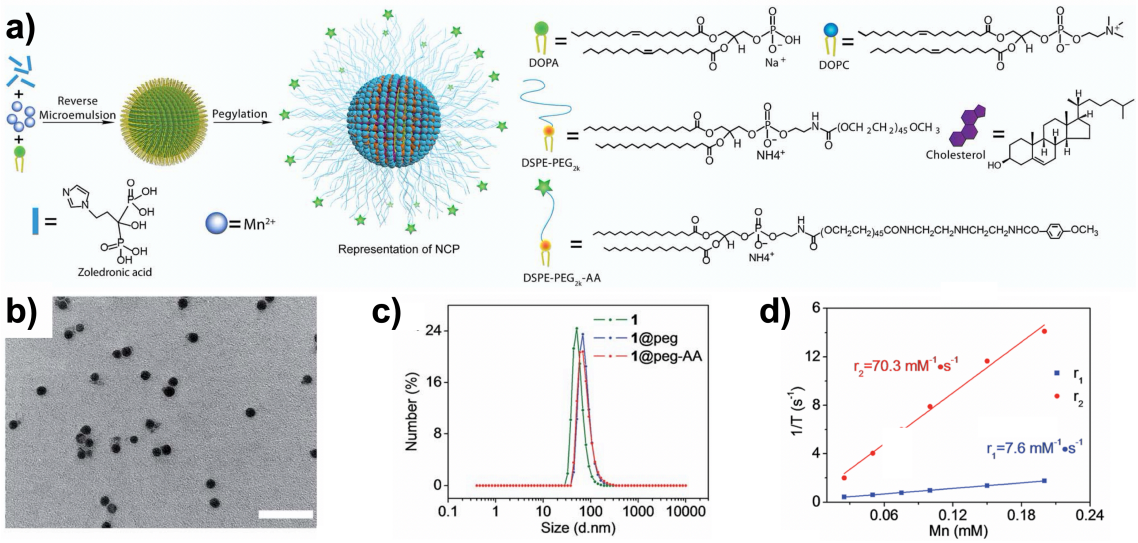

Figure 4. (a) Scheme for the general procedure of self-assembled CPNs with lipid and PEG coating. (b) Transmission electron microscope (TEM) images of Mn-bisphosphonate CPN + peg + anisamide (AA) (1@peg-AA). (c) Size distribution of particles measured by dynamic light scattering (DLS). (d) Longitudinal (r_1, squares) and transverse (r_2, circles) MR relaxivity plots of 1@peg-AA. Scale bars = 200 nm. Adapted with permission from ref. [106], Copyright 2019 Royal Society of Chemistry.

In another work, Yang *et al*. described the synthesis of Mn-CPNs upon self-assembly of Mn^{2+} ions with a near-infrared (NIR) dye (IR825) ligand [107]. The reaction for the CPNs formation was made in methanol/DMF solution containing $MnCl_2$ under sonication for 6 h followed by an additional 12 h of stirring at 30 °C. The resulting NPs were coated with a polydopamine (PDA) layer and subsequently functionalised with PEG molecules, resulting in a final average hD of ~ 70 nm. After applying a magnetic field (3T), the Mn-IR825@PDA-PEG NPs showed an r_1 value of 7.48 $mM^{-1}s^{-1}$, higher than the clinically used Gd-based CA Magnevist®. The *in vivo* results also demonstrated a rapid renal excretion minimising long-term toxicity of Mn^{2+} ions and a gradual uptake by the tumour, which under irradiation, was efficiently removed without any re-growing signal within 60 days. Zhao *et al*. synthesised mesoporous Mn^{2+}-dithiodiglycolic acid (DTA) CPNs (~ 100 nm diameter) loaded with DOX and further PEGylated, using PDA as a primer, that conferred remarkable biostability under physiological conditions [108]. The Mn-based mesoporous NPs were synthesised by mixing $MnCl_2$ and DTA, in

DMF/ethanol solution. Then, the reaction mixture was ultrasonically dispersed and transferred to a hydrothermal synthesis reactor, for 24 h at 150 °C. These NPs showed a concentration-dependent MRI contrast with an r_1 = 9.95 $mM^{-1}s^{-1}$, again higher than the commercial Magnevist®. Moreover, in addition to exhibit improvements in the blood circulation time and the uptake by the tumour after i.v. injection, the NPs have a smart controlled release of the encapsulated DOX. Indeed, the disulphide bonds located in the structure of the DTA could be broken when the antioxidant glutathione was present through redox reactions.

More recently, Zhang *et al*. described the formation of CPNs that encapsulate a photosensitive drug (chlorin e6, Ce6) during the self-assembly process for the formation of the CPNs [109]. The coordination of an amphiphilic amino-acid ligand (9-fluorenylmethyloxycarbonyl-L-leucine, Fmoc) with Mn^{2+} ions at pH = 8.0, yielded the generation of CPNs with an average diameter of approximately 100 nm, as revealed by TEM and DLS measurements. In addition to being biocompatible, the resulting NPs presented a T_1-dominated contrast effect (r_1 = 6.46 $mM^{-1}s^{-1}$) and *in vivo* retention times high enough as for the acquisition of MRI signals within a single scan. On top of that, these CPNs showed strengthening photodynamic therapy (PDT) to treat tumours by controlled releasing of the photosensitiser. Similarly, Shin *et al*. reported a procedure for the coordination of Mn^{2+} ions within pyrene-end-modified double-hydrophilic block copolymers (DHBCs) [110]. The reaction yielded NPs with an hD of 15 ± 4 nm measured in solid-state by TEM. Nevertheless, when the NPS were redispersed in aqueous solution, DLS measurements revealed an increased size of 47 ± 20 nm. This significant difference in diameter dimensions was attributed to the considerable swelling of the Mn^{2+} bond. Moreover, the presence of manganese ions allowed for suitable permeation of water molecules and improved the magnetic resonance relaxivity showing a strong r_1 (17.35 $mM^{-1}s^{-1}$). To close this section, Wu *et al*. reported the development of CPNs through the coordination of methotrexate (Met) chemotherapeutic and Mn^{2+} ions [111]. The resulting CPNs were coated with PEG molecules through hydrophobic interactions. The average hD of Met-Mn NPs from DLS was 81.5 ± 9.7 nm while it changed to 93.3 ± 10.3 nm after the coating of PEG. The presence of Mn^{2+} ions served as T_1 CA with r_1 = 7.76 $mM^{-1}s^{-1}$ while PEGylation enhanced the biostability and the circulation half-lives compared with the free chemotherapeutic (from 0.71 ± 0.15 h to 4.23 ± 1.56 h).

Besides the use of Mn^{2+} ions as constitutive building blocks of the coordination polymer network, Liu *et al*. described the encapsulation of MnO_2 (BM) NPs within CPNs made of hafnium (Hf) and c,c,t–(diamminedichlorodisuccinato)Pt^{4+} (DSP) [72]. The DSP ligand presented double function, acting simultaneously as both bridging ligand and prodrug. The resulting hybrid NPs were further coated with PDA and PEG (BM@CPN(DSP)-PEG), conferring them an excellent water solubility, good physiological stability and an hD of ~ 160 nm. Under acidic pH, the MnO_2 NPs decomposed into paramagnetic Mn^{2+} ions giving different r_1 values with a strong pH/concentration-dependent brightening effect. For this reason, the r_1 at pH = 6.5 was 9.23 $mM^{-1}s^{-1}$, five times higher than at pH = 7.4 (1.75 $mM^{-1}s^{-1}$). On top of that, these NPs act simultaneously as two-faced system. Firstly, as radio-sensitiser due to presence of Hf, this has X-ray attenuation capacity, allowing for excellent therapy and secondly, as chemotherapeutic agent due to the release of cisplatin. This simultaneous effect was corroborated by *in vivo* experiments, showing the enhanced tumour uptake after i.v. injection. Interestingly, an inhibition effect of the tumour growth after the chemoradiotherapy treatment was observed. Furthermore, these CPNs where efficiently excreted through the renal pathway, as tracked by MRI and by biodistribution analysis, with no appreciable *in vivo* toxicity.

Iron

First successful examples of Fe-based CAs were based on iron oxide NPs used to image the reticuloendothelial system [112,113,114]. Nevertheless, there are still some limitations related to iron oxide-based CAs (e.g. interferences with magnetic susceptibility) that dramatically affect the accuracy of the diagnoses and must be addressed before their satisfactory clinical translation [115]. To overcome such drawbacks, the rational design of iron-based CPNs as MRI CAs represented an alternative. One of the most successful strategies followed consists in the coordination of Fe ions with high-affinity phenol-based ligands. Mu *et al*. reported the synthesis of ultrasmall (3-4 nm) gallic acid (GA)-Fe^{3+} CPNs, with good biocompatibility and strong absorption in the visible-NIR region [116]. The reasons to choose phenol-based GA is that these systems exhibit a strong interaction with Fe ions favouring the formation of polymeric networks and have demonstrated excellent anti-tumour effects [117,118]. In this case, the Fe^{3+} ions formed strong coordinative bonds with phenolic and carboxylic groups in GA, Additionally, the functionalisation with bovine serum albumin allowed

for an enhanced stability enabled by the strong coordinating effects between Fe^{3+} and the amide present in albumin molecules. The resulting NPs have low relaxivity values of 0.89 $mM^{-1}s^{-1}$ and 0.95 $mM^{-1}s^{-1}$ for r_1 and r_2, respectively (r_2/r_1 = 1.06) though enough to induce a positive change in the MRI signal of the tumour-bearing mice after *in vivo* antitumoral injection. Moreover, combination with laser treatment (photothermal therapy), allowed not only for the effective imaging but also for the treatment of the tumour. Based on the same principle, Zhang *et al*. reported an added functionality for GA-Fe^{3+} based-CPNs upon its encapsulation within PEG-PLGA structure [119]. Both, modification of the dimensions (final hD of approximately 110 nm as showed by TEM and DLS analyses) and the introduction of a polymeric shell, increased the T_1 contrast efficacy with a higher r_1 value of 10.46 $mM^{-1}s^{-1}$. This enhanced r_1 value suggested this system as a highly efficient T_1 CA. On top of that, the robustness of the approach and the physiological stability and biocompatibility, conferred by the polymeric shell, allowed for its use as MRI guided thermo-chemotherapy. The pH-sensitive behaviour of these CPNs triggered the releasing of GA in acidic environments (**Figure 5**).

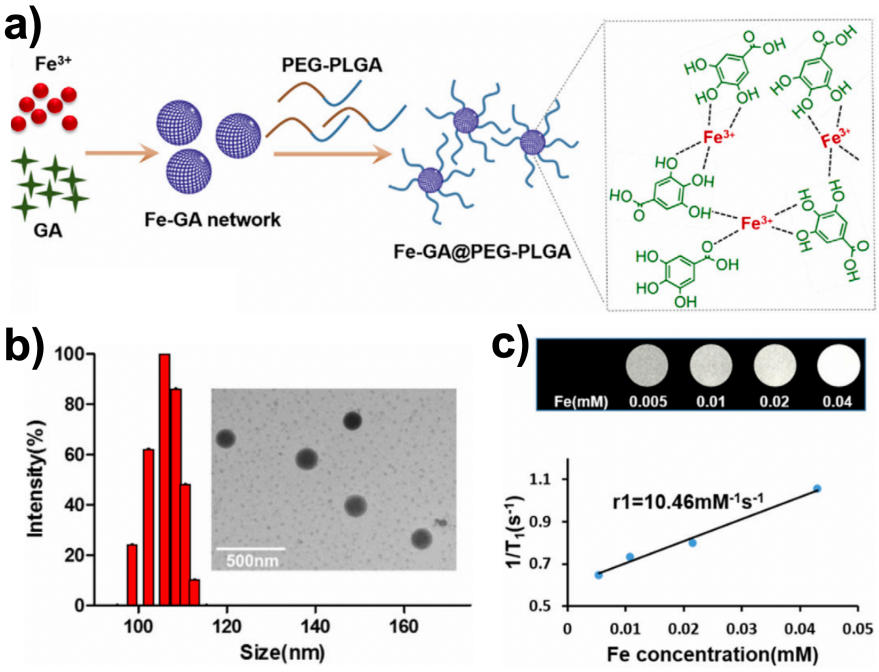

Figure 5. (a) Schematic showing the synthesis and chemical structure of the Fe-GA CPNs (Fe-GA@PEG-PLGA). (b) Size distribution of the Fe-GA@PEG-PLGA CPNs by DLS (Inset: TEM image). (c) T_{1w} MR images of the Fe-GA@PEG-PLGA and the linear fitting for the obtention of r_1 value. Adapted with permission from ref. [119], Copyright 2020 ELSVIER.

As seen before, coordination of active-MRI metal ions to micelles is a successful strategy for the development of nanostructured CAs. Based on this, Xin *et al*. synthesised robust bioinspired catechol-Fe^{3+} coordinated micelles loaded with DOX [120]. The strategy reported allow for the fabrication of catechol-containing amphiphilic polymer conjugate. Interestingly, the conjugate was designed to combine three moieties: catechol, PEG and trityl moieties that enable the polymer amphiphilic and thus endow it self-assembly property. TEM images showed an average size of 74 nm which was increased when the hD was measured by DLS (~94 nm). In this case, the presence of Fe^{3+} showed a low longitudinal relaxivity (r_1 = 1.53 $mM^{-1}s^{-1}$). This low signal, revealed by the MR images under a magnetic field of 1.2 T, did not display noticeable contrast in the tumour region at low concentrations. The low toxicity of this Fe-based CPN allowed for the increase of the injected dose in order to improve the contrast. This image enhancement was possible thanks to a higher accumulation of the system in the tumour surroundings. Besides, the DOX loaded micelles showed a remarkable reduction of tumour size in a 4T1 tumour-bearing mouse. More recently, Qin *et al*. described the formation of bimetal-phenolic CPNs by using Gd and Fe ions, which were crosslinked via metal-catechol coordination with TA [121]. The obtained bimetal CPNs exhibited ultrasmall hD with an average of 23 nm. The r_1 value and photothermal performance of the resulting Gd-Fe-TA CPNs revealed a composition-dependent behaviour. The modulation of the Gd/Fe molar ratio had an opposite impact in both parameters; the r_1 value was positively modified while the photothermal conversion was negatively influenced. Finally, through an accurate optimisation of the Gd/Fe ratio, it was possible to obtain Gd-Fe-TA CPNs exhibiting a high longitudinal relaxivity value (9.3 $mM^{-1}s^{-1}$) and excellent photothermal conversion efficiency in the therapy of EMT-6 tumour-bearing mice.

Dual-mode

Although the possibility of having a dual T_1 and T_2 signal within the same NP has been implicit in many of the previously mentioned examples, some works expressly faced this challenge, giving rise to the so-called T_1/T_2 dual-mode contrast agents (DMCAs). One of the advantages of DMCAs is their capability to be triggered appropriately for their visualisation by bright (T_{1w}) or dark (T_{2w}) images in a single scan, facilitating the interpretation of the diagnostic images and overcoming the MRI artefacts and imaging ambiguities. In recent years, some examples of DMCA-based CPNs have been

successfully synthesised. Yang *et al*. synthesised multifunctional CPNs by a nanoprecipitation method through the reaction between 1,1'–dicarboxyl ferrocene (DCFe) and paramagnetic Gd^{3+} ions [122]. TEM images highlighted the formation of spherical NPs with an average diameter of 80 nm. In a further step, the CPNs were modified with silica to achieve water solubility and surface functionalised with a targeting ligand and tumour specificity. The resulting CPNs were stable in water and did not exhibit significant cytotoxicity. Dual-mode MRI results showed a modest longitudinal relaxivity of $r_1 \sim 5.1$ $mM^{-1}s^{-1}$, similar to Magnevist®, but a significant improvement in the r_2 value (21.7 $mM^{-1}s^{-1}$), four times higher in this case than the commercial Gd-DTPA under the same conditions (5.3 $mM^{-1}s^{-1}$). These values resulted in an appropriate r_2/r_1 ratio ($r_2/r_1 = 4.3$) and suggested the potential use of this Gd-based CPNs as a T_1/T_2 DMCA. In another example, the intrinsic capability of PDA to interact with Fe ions for the formation of DMCAs was reported [123]. In this case, Chen *et al.* reported the synthesis of PDA nanospheres (PDAs) coordinated to the Fe ions as a strategy for the development of biodegradable CPNs (PDAs@CP_3). The strategy consisted first on the formation of PDAs in ammonia/ethanol/water mixture under mild stirring and the addition of dopamine hydrochloride. In a second step, the final CPN was fabricated by a layer-by-layer methodology adding $FeCl_3 \cdot 6H_2O$ to an aqueous solution containing PDAs. The *in vivo* performance showed low toxicity, high biocompatibility and good relaxivity values ($r_1 = 7.52$ $mM^{-1}s^{-1}$, $r_2 = 45.92$ $mM^{-1}s^{-1}$). The resultant ratio $r_2/r_1 \sim 6.11$ $mM^{-1}s^{-1}$, clearly demonstrated the T_1/T_2 DMCA behaviour of these NPs. Moreover, the synthesized nanocomplex was loaded with DOX, allowing for its use in chemotherapy. In this sense, the core-shell nanocomplex was able to reduce the tumour with the controlled release of DOX upon heating.

As showed in the last example, the formation of hybrid nanocomplexes is a robust strategy for the formation of DMCAS. In this sense, Borges *et al*. reported a novel hybrid DMCA through the encapsulation of SPIONs within the catechol-based Fe^{3+} CPNs network [124]. The CPNs were synthesised by combining two co-ligands based on catechol and imidazole under magnetic stirring at room temperature. DLS measurements performed in a solution containing the hybrid nanocomplex (SPION@Fe-CPN) showed an average hD of 86 nm. Interestingly, *in vitro* MRI measurements for the Fe-CPN resulted in an $r_1 = 5.9$ $mM^{-1}s^{-1}$, slightly higher than Magnevist® under the same experimental conditions ($r_1 = 4.25$ $mM^{-1}s^{-1}$). However,

once the SPIONs were encapsulated the r_1 value decreases to r_1 = 2.8 $mM^{-1}s^{-1}$, fact attributed to the localised magnetic field induced by the SPIONs that produced imperceptibly perturbations affecting the relaxation process of paramagnetic-based T_1 CAs. On the positive side, r_2 relaxivity of the SPION@Fe-CPN was equal to 185.3 $mM^{-1}s^{-1}$, allowing for a right T_1/T_2 relaxivity ratio. Later on, Suárez-García *et al*. reported a related DMCA system without the encapsulation of SPIONs, by the combination of imidazole (1,4-bis(imidazol-1-ylmethyl)benzene, bix) and catechol-based ligand (3,4-dihydroxycinnamic acid, dhc) with paramagnetic ions (Gd^{3+}, Mn^{2+} and Fe^{3+}) [125]. This novel family of CPNs were synthesised through a precipitation method induced by the addition of an aqueous solution containing the different metal salts. The resulting CPNs exhibited average diameter sizes ranging from 45 nm (Fe-based CPN) to 130 nm (Mn-based CPN). From all of the different CPNs synthesised, best results were obtained for the Fe^{3+} ions, with $r_1 \sim 5.3$ $mM^{-1}s^{-1}$ and $r_2 \sim 10.9$ $mM^{-1}s^{-1}$ values. These parameters enhanced the corresponding values found for commercial CAs based on Gd^{3+} and Mn^{2+}. Besides *in vitro* experiments, *in vivo* experiments showed an excellent chemical and colloidal stability, low toxicity and good DMCA responses for brain tumour imaging (**Figure 6**). The developed CPNs demonstrated its ability to be accumulated in the tumour environment, thus enhancing the signal and the contrast effect.

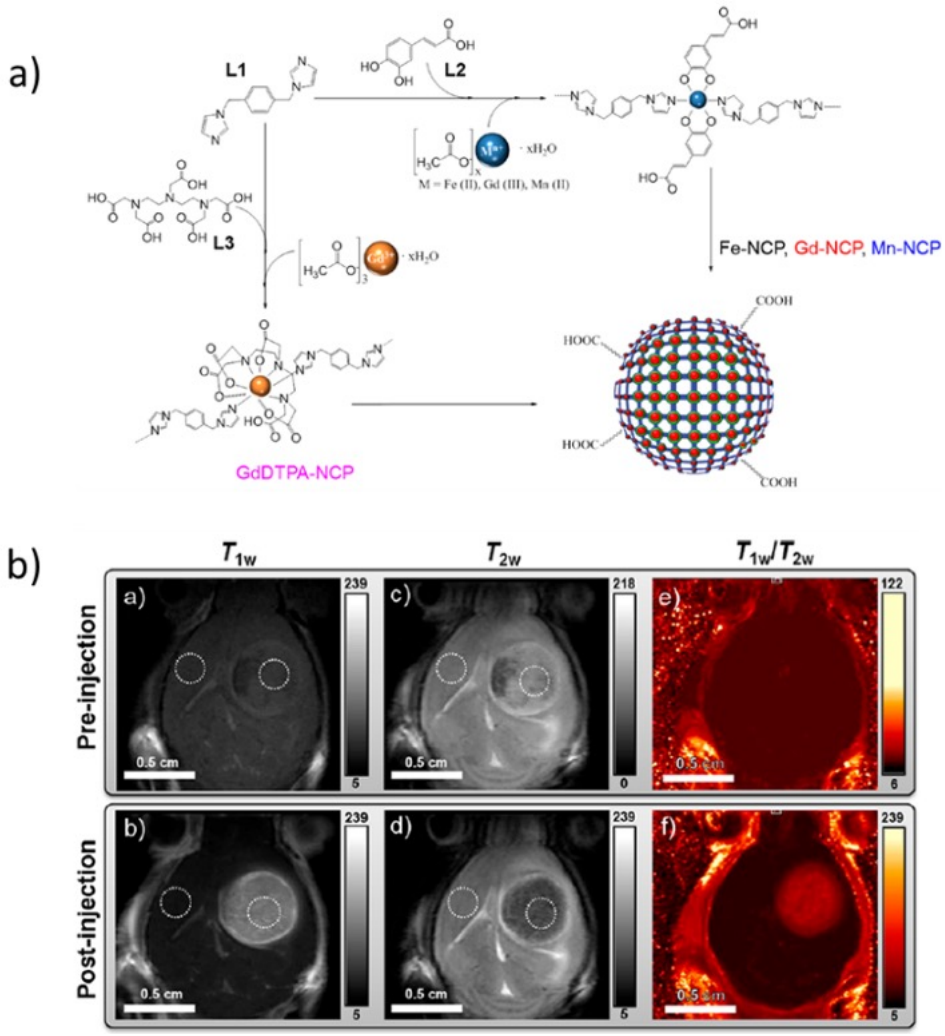

Figure 6. (a) Schematic illustration of the different synthesis for the obtention of a family of CPNs. (b) A representative example of *in vivo* study of GL261 tumour-bearing imaged with Fe-CPN. MR images obtained before injection (first row) and after injection (second row) for T_{1w} image, T_{2w} image and image obtained from an algebra algorithm of imaging division (T_{1w}/T_{2w}). The dashed circles show the selected regions-of-interest (ROIs) for the relative contrast enhancement (RCE) calculation. Colour scales show the range of pixel values in grayscale (for T_{1w} and T_{2w} images) or "hot metal" colour scale (for double enhancement images T_{1w}/T_{2w}), with minimum and maximum values. Adapted with permission from ref. [125], Copyright 2018 American Chemical Society.

In a subsequent example, Solórzano *et al*. modified the previously described Fe-CPNs by introducing an antiviral AZT group in the catechol unit [82]. This modification demonstrated the capability of NCPs to incorporate active therapeutic substances for their controlled release. The resulting CPNs exhibited spherical morphology with hD of 147 nm as demonstrated by DLS. In addition, to show antiviral HIV efficiency with lower side toxicity and controlled release, the CPNs showed a drastic reduction of the r_1 value (0.15 $mM^{-1}s^{-1}$) but a surprising increase of the transversal relaxivity (r_2 = 117.5 $mM^{-1}s^{-1}$). Although the explanation for these differences is not fully understood, it

brings into context the crucial compromise between the use of the ligands and the resultant coordination sphere. This coordination environment will affect the diffusion of bulk water molecules to the metal ions and, consequently, the experimental T_{1w} and T_{2w} responses.

3.2. Computed tomography (CT)

CT is a potent diagnostic tool based on the attenuation of X-ray radiation by the presence of an active element or complex. After signal processing, the resulting 3D images display high quality in terms of spatial resolution. This imaging technique is commonly used in combination with MRI, thanks to the complementary information offered. An active CT CA has to demonstrate high X-ray attenuation, usually materials based on elements with high Z number (e.g. Iodine, z = 53; Barium, z = 56: Hafnium, z = 72 and Bismuth, z = 83; among others). For instance, barium sulphate leads to contrast enhancement used for imaging the gastrointestinal tract. However, and as previous described for other imaging techniques, the use of small-molecule-based CAs is limited due to their I) non-specific biodistribution, II) rapid clearance from the organism through the renal pathway, III) low blood circulation times and IV) the need of large doses for providing quality contrast [126]. For these reasons, many efforts have focused on the formation of nanostructured polymer systems that overcome the above limitations. With this aim, deKrafft *et al*. described the formation of five novel CPNs by reaction of 2,3,5,6–tetraiodoterephtalic acid (I_4-BDC-H_2) with Cu^{2+} and Zn^{2+} ions with excellent X-ray attenuation activity [127]. The described approach established a strategy for the formation of CPNs not only using organic solvents, but also water, which is more suitable for biomedical applications. The resulting CPNs had rod-like morphology, but under an accurate control of the reaction parameters, NPs ranging from 200-600 nm could be obtained. Interestingly, the iodine content of these CPNs (63 wt%) was higher when compared with Iodixanol (49 wt%), a clinically available CA. This high payload together with the biodegradability nature of CPNs, allow for its potential use for imaging applications. In a further example, Liu *et al.* described a remote-controlled drug release CPN formed by the polymerisation of a bis–(alkylthio) alkene linker (BATA) and Hf^{4+} ions [128]. In a first step, the CPNs were produced based on the coordination between Hf^{4+} ions and BATA linker via solvothermal method in a solvent mixture of DMF/ethanol. Interestingly, the resulting NPs, with average diameter

of around 70 nm, were loaded with the photosensitiser Ce6 and the chemotherapeutic drug DOX. Finally, the developed CPNs were PEGylated to confer enhanced stability. *In vivo* CT imaging showed efficient tumour accumulation after i.v injection and enhanced contrast compared with untreated mice. The CPNs were able to produce singlet oxygen upon red light exposure, thereby triggering DOX release due to BATA cleavage and destruction of the NPs. This smart-responsive material resulted in an efficient system for cancer therapy achieved by a combination with chemo-PDT. Additionally, the formation of the CPN allowed for the reduction of toxicity compared with Iopromide, which is a commercial iodine-based CA.

3.3. Optical Imaging (OI)

OI has demonstrated powerful capabilities as a versatile imaging tool. The success of OI technique relies on its non-invasive nature and the ability to discern between healthy and damaged tissues both *in vitro* and *in vivo*. Most nanostructured optical bioimaging agents reported so far are based on Quantum Dots (QDs) and derivatives. These systems have demonstrated photochemical and metabolical stability and tuneable emissions [129,130,131,132,133,134]. Nevertheless, serious concerns about the chemical stability (e.g. oxidation) and toxicity in water have been reported [130,135]. For this reason, many efforts have been focused on the development of CPNs as an efficient alternative. With this idea, Zhang *et al*. reported the formation of ultrasmall CPNs made of Zn^{2+} and 3,4,9,10–perylene-tetra carboxylate [136]. The ultrasmall size of these quantum dots-based CPNs (around 3.0 nm as shown by TEM) ensured their colloidal stability in water. The optical characterisation revealed high photoluminescence and robust photostability. The CPNs were validated *in vitro* by labelling A498 cells, exhibiting similar performances to those of common inorganic QDs (enhanced with respect those reported for commercial fluorescent dyes). Furthermore, the low toxicity of the systems was corroborated *in vitro,* demonstrating the biocompatibility.

Simultaneously, Zhong *et al*. developed lanthanide hollow spheres using Tb ions and the 4,4',4''–benzene–1,3,5–triyl–tri–benzoic acid (BTB) ligand under solvothermal conditions [137]. The resulting CPNs exhibited sizes ranging from 260 to 500 nm in diameter, as shown by scanning electron microscopy (SEM). Interestingly, the use of Eu^{3+} at different doping concentrations allowed for multicolour emission (from green to

red). Worth to mention, excitation of the system at 316 nm allowed for the obtaining of white-light emission, which is a current challenge due to increasing energy demands and subsequent costs. Similarly, Aimé *et al*. also described a new method based on the inclusion of guest molecules to produce photofunctional nucleotide–lanthanide systems [138]. The synthesis was done in water through the mixing of 2'–deoxyadenosine 5'–monophosphate (DDM) and Tb^{3+} ions, forming aggregated CPNs with an hD ~ 30 nm. Once the system was excited at a wavelength of 260 nm, no emission was detected, mainly due to the lack of energy transfer from adenine to the metal ion. In order to obtain optically-active CPNs, 3–hydroxypycolinic acid (hPA) was added to the reaction mixture. This addition allowed for the diffusion of water molecules in the Tb^{3+} coordination sphere inducing the replacement and favouring the luminescence of the CPNs.

Optically active ligands

Instead of photoactive metal ion nodes, an alternative approach for the synthesis and design of photoactive CPNs is the use of fluorescent bridging ligands, such as the well-known meso–tetrakis(4–carboxyl)–21H,23H–porphyrin (TCPP). With this in mind, Liu *et al*. reported the synthesis of CPNs from a microemulsion method by the coordination between Zr ions and the TCPP ligand [139]. The fine tuning of different parameters aroused in the formation of CPNs with different morphology. Among them, spindle-like CPNs (155x260 nm) were selected as the final system for *in vivo* assays. After excitation at 514 nm, the free TCPP ligand exhibits fluorescence at 651 nm (with a low intense peak at 710 nm). Interestingly, nanostructured CPNs revealed a single-emission peak at 689 nm, fact ascribed to the hybridisation between the orbitals of Zr ions and TCPP ligands. Additionally, the CPNs have been efficiently tested for the treatment of tumour, thanks to the combination of laser irradiation and the controlled encapsulation-release of DOX. Besides TCPP, other bridging ligands have demonstrated its effectiveness in OI. Lin and co-workers used the optical-active $Ru(bpy)_3^{2+}$ derivatives to coordinate Zn or Zr ions to synthesise a family of phosphorescent CPNs [140]. The resulting CPNs were stabilized by performing a coating of silica. However, only the Zr-based CPNs showed enough stability without decomposition in water. This system was selected for further functionalisation with PEG molecules (through silanol and siloxy groups). Finally, the tumoral specificity of these CPNs was validated *in vitro*, showing their uptake by H460 cells as demonstrated by confocal microscopy.

In another example, Ban *et al*. synthesised Cu-containing amphiphilic hyperbranched polytriazoles following self-assembly processes with very low cytotoxicity [141]. First, Cu^{+}-catalysed azide-alkyne cycloaddition polymerysation was used to produce hyperbranched polytriazoles which were subsequently functionalised with alkyl-modified PEG. The average hD of these assemblies was 75 nm with spherical shape. The resulting system allowed for their use as active-fluorescent CPNs due to aggregation-induced emission phenomena (AIE). For instance, optical analysis of the CPNs as a solid powder revealed a wide range of emissions (cyan, yellow, and red–light) while dispersed in aqueous solution, the emission changes to intense blue, yellow-green, and dark red-light under the same irradiation parameters. Worth to mention, this system also unveils a responsive behaviour thanks to the presence of disulphide bonds, which lead to release the antitumoral fragments of copper-triazole complexes. In another example, Heck *et al*. described phosphate-based hybrid NPs (IOH-NPs) combining various amounts of inorganic cations ($[ZrO]^{2+}$ or $[Mg_2O]^{2+}$) and a functional (e.g. fluorescence or drug release) organic anion $[R_{function}(O)PO_3]^{2-}$ (**Figure 7**) [142]. The formation of this novel family of CPNs was based on the fact that functional organic anions comprising phosphonate or phosphate groups, commonly turn into insoluble salts on addition of $[ZrO]^{2+}$ or $[Mg_2O]^{2+}$ cations. With this methodology, several types of NPs ranging from 20 to 40 nm (as shown by SEM) were synthesised. Depending on the different combinations and the fluorescent dye anion selected, the CPNs showed blue, green, red, and NIR fluorescence. Other alternatives tested consisted on the use of active molecules with antitumoral activity (e.g. FdUMP = 5′–fluoro–2′–deoxyuridine 5′–monophosphate), showing high payloads.

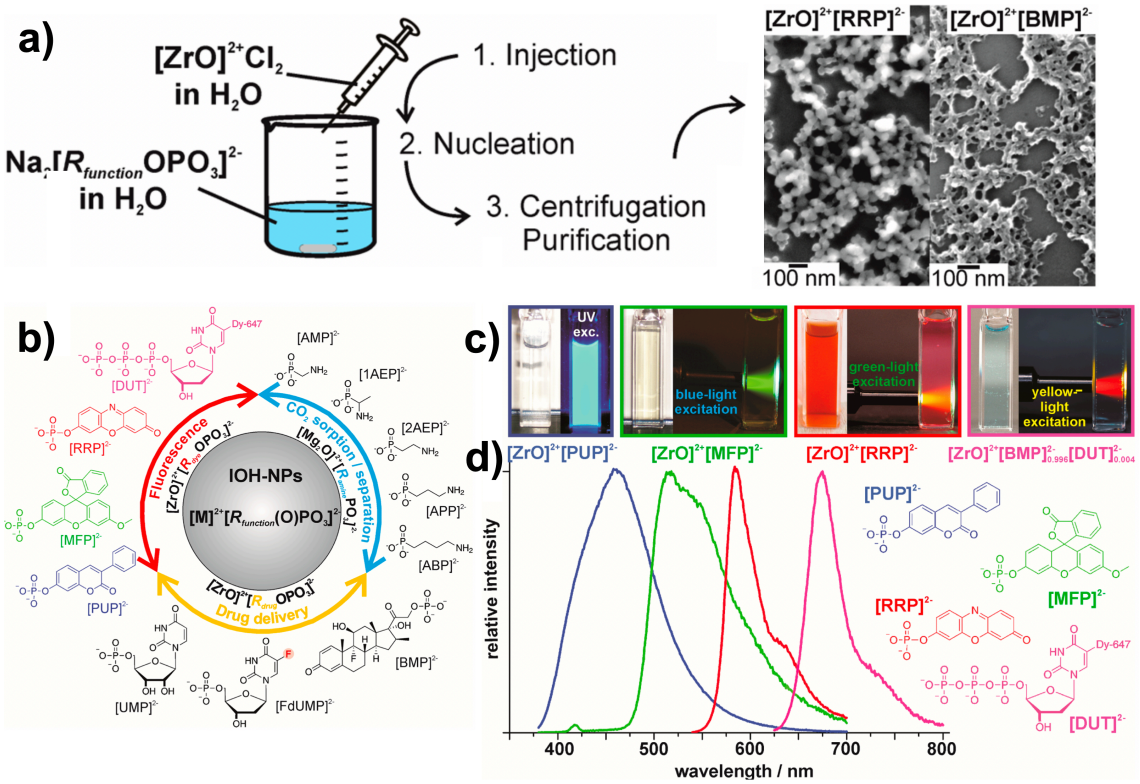

Figure 7. (a) Synthesis of inorganic-organic hybrid NPs (IOH-NPs) and corresponding SEM images. (b) Manifold combinations and multipurpose properties of the IOH-NPS $[M]^{2+}[R_{function}(O)PO_3]^{2-}$ (M = ZrO; Mg_2O; R = functional group). (c) Different IOH-NPs in aqueous suspensions. (d) Emission spectra and chemical composition. Adapted with permission from ref. [142], Copyright 2015 American Chemical Society.

Alternative functionalisation

Beyond those metal ions and/or organic ligands that are already an intrinsic part of the polymeric structure, alternative functionalisation consists in the incorporation of additional optical dyes within the NPs. Taking this into account, Sahub *et al.* synthesised colloidal stable CPNs based on the coordination of Gd^{3+} metal ions with the $-SO_3^-$ and −OH groups present in the sodium dodecyl sulphate (SDS) and 4–(2–hydroxyethyl)–1–piperazineethanesulfonic acid (HEPES) [143]. Then, a solution containing $Gd(NO_3)_3$ DMSO was added into a solution of SDS-HEPES giving a colloidal suspension of NPs with average size of 60 nm, as shown by TEM images. Interestingly, the encapsulation of two curcuminoids (Cur and $CurBF_2$) enhanced the fluorescence quantum yield compared to the free curcumin derivatives. This improvement could be related to both the confinement of the packed dye molecules and an increase of the cellular uptake. Another route for incorporation of optically active molecules consists in the functionalisation of the surface with dyes. In this sense, Novio

et al. synthesised Fe- and Co-based CPNs with catechol ligands, bearing pendant carboxyl groups, and imidazole-based coligand to induce the polymerisation [45]. The ligands were dissolved in ethanol and subsequently addition of metallic salts ($(CH_3COO)_2 \cdot xH_2O$, were x = Co or Fe) in water (antisolvent) induced the precipitation of CPNs. SEM and TEM images revealed spherical NPs with an average diameter of about 110 nm (Co-based CPN) and about 94 nm (Fe-based CPN). The $-CO_2H$ groups exposed outside of the CPNs were used for the attachment of 6–amino fluorescein (ANF) dye. The monitoring of the fluorescently-labelled CPNs performed by a confocal laser scanning microscopy (CLSM) on MCF7 cells, lead to the localisation of the CNPs inside the cells, with a cellular internalisation of 27% and 39% for the ANFCo-CPN and ANFFe-CPN, respectively. The mechanism involved in their internalisation consisted mainly in the endocytosis pathway due to the negative surface character of these NPs originated by the superficial carboxylic groups.

In another approach, to track the cell internalisation of self-assembled zinc-bisphosphonate CPNs, Liu *et al*. added a small fraction of rhodamine B (rhod B) to afford rhod B-doped CPNs [144]. In this case, two different Zn-based CPN systems were synthesised: one containing the cisplatin and the other one the oxaliplatin prodrug. The CPNs were produced through a reverse microemulsion method. TEM images showed the formation of spherical NPs with an average diameter about 25 nm. In a final step, both systems were PEGylated in order to enhance the colloidal stability and biocompatibility. Accordingly, CLSM showed the efficient internalisation of the NPs by CT26 cells through endocytosis and fluorescence imaging from Ce6-doped CPNs was achieved for the *in vivo* study of CT26 tumour-bearing mice. Interestingly, the loading of these CPN platforms with the prodrugs, allowed *in vivo* antitumor activity significantly more effective than the free drugs. The same group reported later on a modification of Ce6 doped Zn-based CPNs to incorporate oxaliplatin and gemcitabine monophosphate (GMP), which are well-known chemotherapeutic agents [145]. Using confocal imaging studies, the integration of the CPNs in the cytoplasm was demonstrated, allowing for the *in vitro* pharmacokinetic study. As we have seen, the encapsulation of optical-active dyes within CPNs is a useful strategy. This approach is being used more frequently with the objective to endow CPNs with imaging activity. Recently, in 2020, Pen *et al.* reported the formation of Cu^{2+}-based CPNs for optical imaging and specific cancer therapy [146]. The CPNs were prepared based on the

coordination between Cu^{2+} ions and dithiocarbamate (DTC) ligand under mild conditions. The self-assembly process yielded the formation of spherical NPs, which were coated with hyaluronic acid using electrostatic interactions. TEM images showed an average diameter about 100 nm before and 125 nm after the surface modification. Then, the encapsulation rhod B and Ce6 was performed and their corresponding drug-release profile exhibited a sustained release. Finally, the CPNs loaded with Ce6 were injected in mice. Interestingly, the fluorescent signal showed a passive accumulation in the tumour tissues after 24 h. Overall, these results suggested the potential use of these CPNs as suitable drug-delivery system and effective nanoplatform for tumour therapy.

Dual-mode

Another area of research has been the development of dual-fluorescent CPNs for their use in multichannel imaging mode. With this objective, Nador *et al*. reported the formation of Co-based CPNs via precipitation method, which were functionalised following two different strategies (**Figure 8**) [147]. In the first of such approaches, the surface of CPNs containing two different catechol ligands (dopamine ($–NH_2$ terminal group) and 3,4–dihydroxybenzldheyde (–CHO terminal group)) was covalently functionalised with fluorescein isothiocyanate (FITC), 1–pyrenebutanoic acid hydrazide (PBH) and Alexa Fluor® 568 (A568). In the second strategy, the pre-functionalisation of phenol-based ligands with the corresponding dyes takes place before the formation of the CPN. If we compare the performance of both systems, the first route allowed for the incorporation of ~ 3% w/w of dye with accurate control over their emission properties and final morphology of the NPs. However, the second strategy offered higher dye payloads but less control over the final morphology and size of the CPNs. Finally, the internalisation of the CPNs by HeLa cells was confirmed by CLSM, and the stability of such dyes after uptake was probed after measuring the cellular fraction. This methodology allows for the production of functionalisable CPNs with a wide variety of dyes. Interestingly, the correct combination of different fluorescent moieties in a single platform, make affordable the use of CPNs for simultaneously detection through visible to NIR wavelengths.

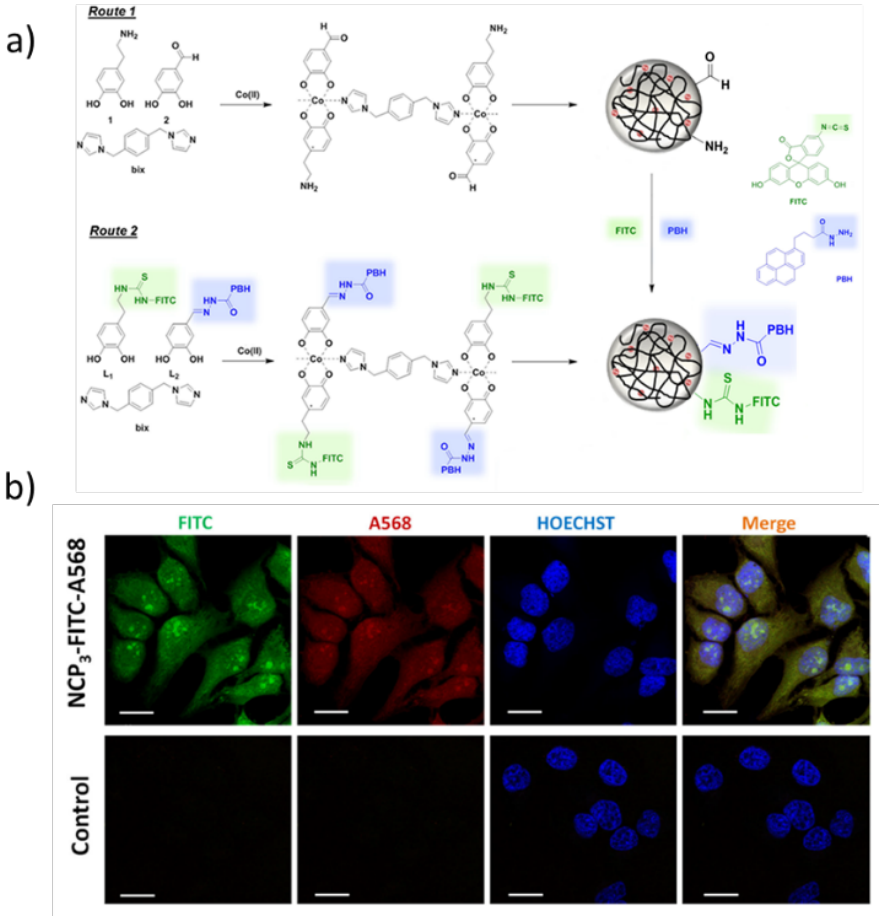

Figure 8. (a) Synthetic scheme of the two different pathways followed for the preparation of dual-fluorescent CPNs. (b) *In vivo* images (CLSM) of HeLa cells after incubation for two hours with CPN3-FITC-A568 and the corresponding control (non-functionalised CPN). Individual channel projections are used to track the localisation of FITC (in green), A568 (in red), the nuclear stain (Hoechst, in blue) and finally the superposition of all channels (merge). Scale bars are 20 mm. Adapted with permission from ref. [147], Copyright 2018 Wiley.

Stimuli-responsive

As seen in other examples of the use of CPNs for bioimaging, one of the most advantageous features is to produce platforms that respond in a certain way (e.g. bond cleavage) under a certain stimulus (e.g. pH). In this sense, Li *et al.* reported NPs made of Zn^{2+}, Ce6 and a His derivative with sensitive responses to pH and redox stimuli [71]. The high affinity of His to coordinate metals was used for the self-assembly of Zn-based CPNs. The nanoplatforms were obtained via precipitation method yielding CPNs with average size about 75 nm, as confirmed by DLS. The Ce6 photosensitiser was incorporated exhibiting a capacity loading higher than 50% with encapsulation efficiency above 99%. This high payload and efficiency was attributed to the fact that Ce6 participated in the formation of the CPNs through cooperative coordination. The *in vivo* distribution, tracking of the NPs in tumour-bearing mice using fluorescence

imaging, showed a preferential accumulation and an efficient photodynamic ablation of tumours, without off-target side effects. Additional examples include the nanoplatform described by Liu *et al*. based on Hf^{4+} and an imine- pH-responsive linker [62]. In this specific case, the Hf metal ions were used as radiosensitisers for enhanced tumour radiotherapy while labelling with a fluorescence dye (1,1′–dioctadecyl–3,3,3′,3′–tetramethylindotricarbocyanine iodide) allowed tracking the cellular uptake by confocal fluorescence microscopy. The CPNs were prepared through a reverse microemulsion yielding NPs with average diameter about 280nm. The presence of pH-responsive benzoic-imine linker allowed for the controlled release of therapeutic moieties. At the *in vivo* level, the developed CPNs were i.v. injected, showing high tumour uptake in mice. Remarkably, once the tumour was treated with the CPNs, the size was reduced after X-ray radiation.

In a last example, Yang *et al*. similarly reported a series of nanoplatforms formed by dicarboxylic cisplatin (IV) prodrug (linker), poly–L–His–PEG (stabilizer) and a metal cation (Ca^{2+}), exhibiting excellent accumulation in the tumour and high responses to pH changes [64]. The CPNs were synthesised through a one-pot reaction yielding NPS with spherical morphology and average hD about 50 nm. The pH-responsive behaviour of these CPNs induced a charge switch, allowing for decomposition of the nanoplatforms and release of cisplatin. After doping the CPNs with indocyanine green (ICG), a NIR dye, fluorescence imaging was used to *in vivo* track the biodistribution of CPNs in 4T1 tumour-bearing mice. The results demonstrated the successful use of these CPNs as a chemotherapeutic agent, particularly under acidic pH.

3.4. Radioimaging (RI).

Radionuclide imaging offers a potent tool for the detection, imaging and monitoring of different diseases in fields such as oncology, neurology, metabolism, inflammation and musculoskeletal system [148,149,150,151]. Positron emission tomography (PET) and single-photon emission computed-tomography (SPECT) imaging present some advantages compared with other imaging techniques: I) better detection sensitivity (at the picomolar range), II) higher penetration depth (in particular comparing with optical imaging) and III) wider quantitative scope [152]. The risks of the technique are implicit in the use of radiotracers that researchers must face efficiently, especially considering

the risk of NPs to be retained in the reticuloendothelial system organs. Usually, radiometals suitable for PET/SPECT imaging are used as stable complexes with different chelating molecules [153]. Selection of the chelator must be specific, considering the physicochemical properties of the radiometal (oxidation state, coordination number and kinetic reactivity, among others). Moreover, most of the strategies currently developed are focused on the production of chelator-free radiotracers, avoiding tedious synthesis procedures. In this scenario, CPNs may be good candidates for the inclusion of radiometals in a safer strategy, allowing the formation of predesigned systems with excellent biocompatibility, biodegradability and, therefore, overcoming their potential risks.

In 2014, Oh *et al*. reported the first example of a CPN that incorporated a radiotracer in its network [154]. In this work, CPNs with average diameters of 5-7 nm were obtained by the coordination polymerisation of an imidazole-based ligand and a gamma-emitting radionuclide (^{198}Au). The success of the methodology was corroborated with other ligands though the lack of *in vitro* and *in vivo* studies makes it impossible to know their behaviour in biological environments [155]. Later, Shen *et al*. reported the one-step synthesis of renal-clearable ultrasmall CPNs formed by coordination of W^{4+} ions with GA as bridging ligand [156]. Due to the high affinity between the phenolic hydroxyl groups of GA and metal ions, CPNs could efficiently be labelled with $^{64}Cu^{2+}$ via a chelator-free strategy. Afterwards, the NPs were further PEGylated fact that, together with their ultra-small size (1-2 nm), helped to the rapid and effective renal clearance, avoiding long-term side effects. On top of PET imaging, and thanks to the tungsten radio-sensitising with strong X-ray absorption, these CPNs greatly enhanced the efficacy of cancer radiotherapy by inhibiting the tumour growth. More recently, in 2018, Lu *et al*. reported the loading of CPNs with ^{64}Cu for PET imaging by encapsulating phthalocyanines in water-dispersible PEG-coated NPs under mild conditions [157]. The CPNs were produced via flash nanoprecipitation, which is a methodology consisting in the dissolution of lipophilic materials and stabilizing block copolymers in water-miscible organic solvents. This mixture is rapidly combined against an aqueous stream to induce the nucleation and growth of lipophilic material into NPs. This strategy is a versatile approach for the encapsulation hydrophobic moieties into water-dispersable NPs. The resultant NPs were obtained with a relatively wide size distribution (from 70 to 160 nm) though still within limits required in medical

applications. The developed CPNs could be stored and subsequently incubated with ^{64}Cu immediately before to performing the imaging scan. Interestingly, the radiochemistry yield achieved was also high, reporting values >90% of radionuclide chelation.

The use of ^{99m}Tc has been widely employed in clinical SPECT radioimaging mainly due to its short half-live (6.01 h) and rich chemistry that allows its bonding to a variety of biochemical compounds. In this context, Yang *et al*. reported the formation of CPNs prepared by the coordination between Ca^{2+} ions and AS1411 DNA G-quadruplexes (Ca-AS1411 CPNs) [158]. This novel nanostructure allowed for the insertion of different active molecules such as the photosensitiser Ce6 and hemin (Fe-containing porphyrin). This strategy favoured the generation of reactive oxygen species inside cell nuclei upon 660 nm irradiation. However, a low signal-to-noise ratio and the self-quenching effect of the photosensitiser, endangers the possible use of the fluorescence imaging to obtain the *in vivo* distribution of NPs inside animals. For this reason, ^{99m}Tc, with strong γ-ray emission, was efficiently introduced through its chelation in the centre of the porphyrin rings without needing additional chelator agents. The resulting CPNs exhibited spherical morphology and average size distribution centred at 70 nm. The *in vivo* tracing in 4T1-tumour-bearing mice showed contrast in a time-dependent manner. In another example, Chao *et al*. described the one-pot formation of PEG-modified CPNs composed of Hf^{4+} and TCPP (**Figure 9**) [159]. The formation of Hf-TCPP-PEG CPNs allow for its labelling in high yields with ^{99m}Tc thanks to the chelating structure of TCPP. The CPNs were produced through a one-pot reaction by mixing the ligands and the metal ions. The resulting CPNs showed an average hD about 70 nm with high colloidal stability. Interestingly, Hf was able to eliminate cancer cells because its interaction with the γ rays originated from ^{99m}Tc. Therefore, these ^{99m}Tc-Hf-TCPP-PEG CPNs showed efficient tumour retention with outstanding therapeutic features in eliminating tumours after moderate doses of ^{99m}Tc. Remarkably, these CPNs resulted easily biodegraded and excreted, avoiding long-term body retention.

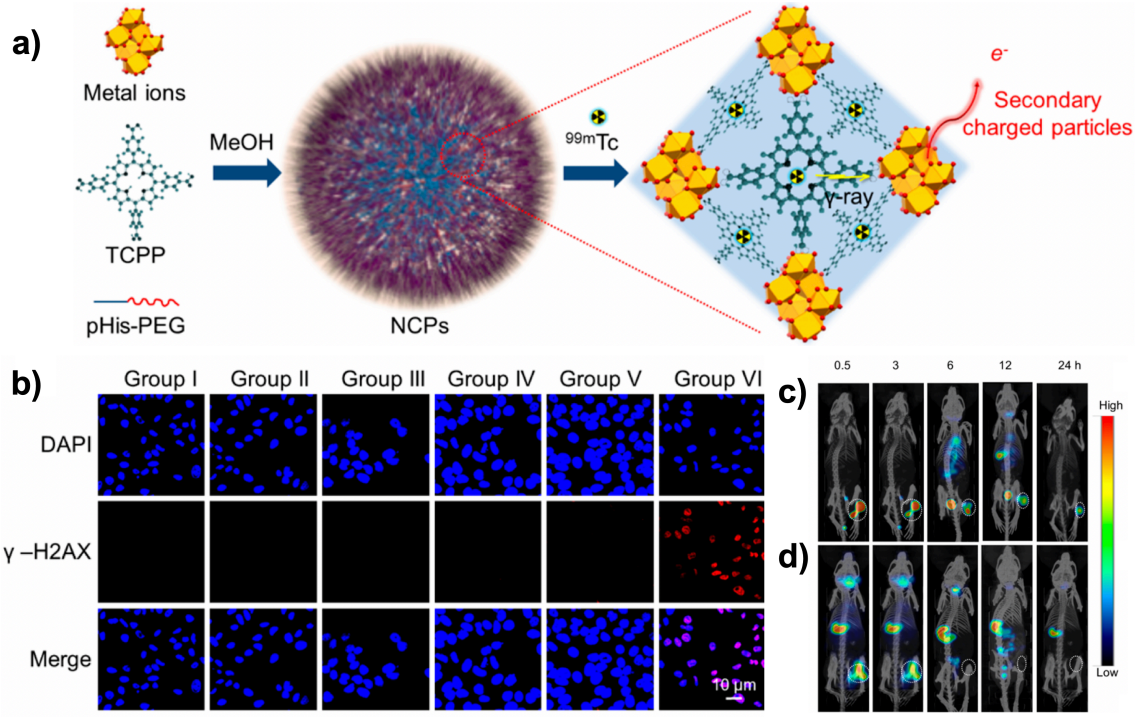

Figure 9. (a) The Scheme shows the formation of Hf-TCPP-PEG CPNs and additional radiolabeling with 99mTc, as well as the generation of secondary charged particles by Hf after absorbing γ rays emitted from ^{99m}Tc. (b) Confocal fluorescence images of γ-H2AX-stained 4T1 cells after various treatments for 24 h. Blue, DAPI; red, γ-H2AX. Groups I, II, III, IV, V, and VI stand for saline, Ca-TCPP-PEG, Hf-TCPP-PEG, free ^{99m}Tc, ^{99m}Tc-Hf-TCPP-PEG, and ^{99m}Tc-Hf-TCPP-PEG, respectively. (c,d) *In vivo* SPECT images of 4T1 of rodents after intratumoral local injection with ^{99m}Tc -Hf-TCPP-PEG CPNs (c) or free ^{99m}Tc (d). Adapted with permission from ref. [159], Copyright 2018 American Chemical Society.

3.5. Photoacoustic imaging (PAI)

Photoacoustic imaging (PAI) is a technique based on the irradiation and absorption of biological tissues with non-ionising laser pulses that is transformed into heat. Such heat induces a thermal expansion associated to acoustic waves, which are detected by ultrasonic transducers and transformed into images. PAI as a hybrid non-ionising imaging modality provides deep tissue penetration as compared with optical imaging due to the minimised scattering of acoustic waves relative to light [160,161]. This imaging modality is used to understand fundamental biology such as imaging of diseases biomarkers [162,163], brain imaging [164,165], angiogenesis [166], and cancer diagnostics [167]. However, as PAI signals are generally lower than optical imaging signals [168], imaging agents with high photoacoustic brightness are required. Most of the used PAI probes are based in organic dyes [169], fluorescent proteins [170], gold nanoparticles [171], carbon nanotubes [172], 2D materials [173], up-conversion nanoparticles [174] and semiconducting polymer nanoparticles [175,176,177].

With respect to CPNs, not many examples have been so far reported. Only recently, Wang *et al*. described the synthesis of a complete set of Fe^{3+}-based NPs using phenolic ligands with different structures (nophenol: resorcinol and hydroquinone, orthodiphenol: pyrocatechol and 1,2,4–trihydroxybenzene (DB), and ortotriphenol: pyrogallol (PG), GA, epigallocatechin gallate (EG) and TA) [178]. The family of CPNs were synthesised using a single one-step method and PVP as a stabiliser and protective agent. The resulting nanostructures showed different diameters ranging from 5 to 60 nm, as shown by TEM images. In almost all the cases, the developed CPNs demonstrated good biocompatibility and biosafety, effective for *in vivo* applications. In particular, Fe^{3+}-TA complex exhibited suitable dimensions for tumour accumulation. Interestingly, this CPN complex presented strong UV-vis absorbance, high photothermal capacities and PAI compared to Fe^{3+}–nophenol, orthodiphenol and orthotriphenol complexes. Fe^{3+}-pyrocatechol and Fe^{3+}-TA systems similarly featured excellent photothermal performance and antitumor effect on MCF7 cells with laser irradiation. Therefore, the photothermal properties and PAI performance of Fe^{3+}-phenolic complexes resulted optimal for PAI-guided PTT, thus opening a novel theranostic application for CPNs.

3.6. Bi- and Tri-modal Imaging

In this section, examples of CPNs that allow for their simultaneous imaging with different diagnostic techniques will be discussed. The combination of more than one imaging technique in a single platform facilitates the interpretation of the diagnostic images, thus overcoming artefacts and imaging ambiguities. The multimodality imaging CPNs have been grouped by families embracing the same combination of techniques, as described next.

MRI/CT + OI

This combination of techniques is probably the most successfully used by CPNs, which indistinctly allows for their visualisation by MRI and OI. In this context, Zhou *et al*. reported CPNs incorporating phosphorescent carboxyl-functionalised Ir^{3+} complexes and magnetic Gd^{3+} [179]. The nanostructures were hollow spheres with an average diameters and wall thickness of 60 nm and 10 nm, respectively as revealed by TEM images. The CPNs were also mixed with PVP to improve their colloidal stability. The

produced low cytotoxic nanosystems (with hD ~ 195 nm) showed relative stability in water and PBS at room temperature with strong red phosphorescence. The presence of Gd^{3+} ions in the CPN network allowed for the detection of modest longitudinal relaxivity (r_1 = 8.0 $mM^{-1}s^{-1}$) and significant transverse relaxivity (r_2 = 10.8 $mM^{-1}s^{-1}$). Moreover, coupled plasma atomic emission spectroscopy and CLSM assured their uptake in living cancer cells. In another example, Lu *et al*. also described water-soluble CPNs built with Ir^{3+}, Gd^3 and 2–2'bipyridine–3.3'–dicarboxylic acid [180]. The CPNs were produced through a coordination assembly and by adding PVP to enhance the NP stability. The TEM and SEM images revealed the formation of NPs with average size about 150 nm which was increased up to 270 nm when measured in DLS. This increase in size was attributed to the formation of aggregates in aqueous solution. The synthesised CPNs showed absorption in the visible region (560 nm) and high longitudinal relaxivity (r_1 = 29.5 $mM^{-1}s^{-1}$). Interestingly, the CPNs exhibited low cytotoxicity and excellent stability in simulated biological environments. Overall and thanks to its successful internalisation (as confirmed by CLSM), $^1O_2$ generated after irradiation with visible light was effectively employed for the PDT of cancer cells.

Wang *et al*. synthesised multifunctional Gd-Yb CPNs using $Ru(bpy)_3^{2+}$ as a fluorescent ligand [181]. The CPNs were synthesised by following a microemulsion method, yielding NPs with diameters about 130 nm. Through an accurate optimisation of Gd/Yb ratio, the CPNs successfully integrated the red fluorescence and the $^1O_2$ production of the Ru-ligand, paramagnetic MRI-activity of Gd^{3+} and the high attenuation of Yb^{3+}. Indeed, both UV-vis absorption and fluorescence emission of the CPNs showed a wide absorption band at 480 nm and a high red fluorescence at 655 nm. The red emission of the CPNs lies in the transparent biological range, avoiding the disturbance from the autofluorescence and scattering light of tissue by minimising background imaging. The *in vitro* relaxivities measurements showed a high r_1 = 26.27 $mM^{-1}s^{-1}$, which is 7-fold of commercial GdDTPA, indicating the ability of the system to act as T_1 CA. The performance of this multiplatform was finally tested *in vivo*, confirming its high imaging and PDT efficiency (**Figure 10**). Interestingly, the inclusion of Yb was effective for the acquisition of CT imaging with remarkable signal enhancement. Therefore, these CPNs could be used as a CA for optical, MRI and CT triple-modality imaging.

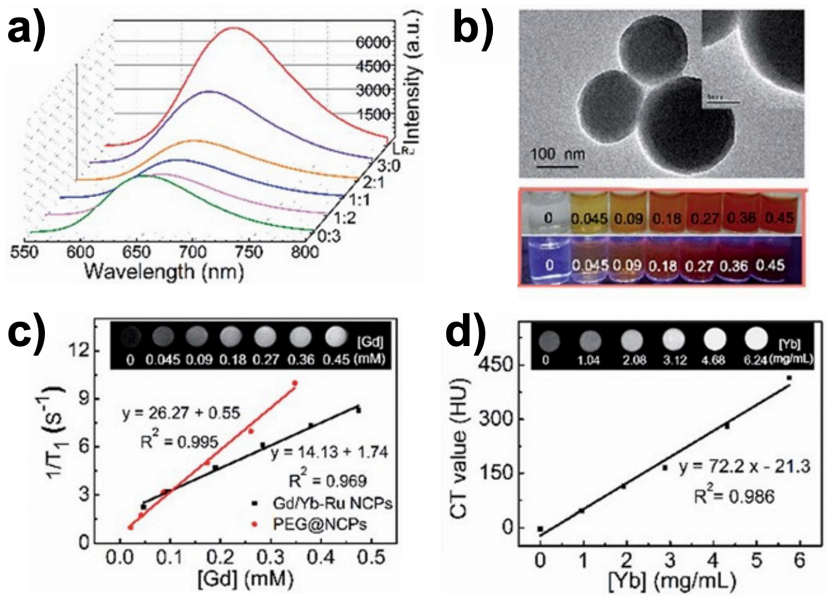

Figure 10. (a) Fluorescence spectra of Ru–based ligand and CPNs with diverse Gd/Yb ratios. (b) T_{1w} MR and CT images of the CPNs with different Gd/Yb ratios and water. (c) TEM images of PEG@CPNs (up) and photographs of PEG@CPNs aqueous solutions upon sunlight and irradiation at 365 nm (bottom). (c) r_1 relaxivity curve of the PEG@CPNs and Gd/Yb-Ru CPNs. Inset: T_{1w} images of the PEG@CPNs in different concentrations. (d) CT attenuation plot of the PEG@CPNs. Inset: CT image of the PEG@CPNs in different concentrations. Adapted with permission from ref. [181], Copyright 2017 Royal Society of Chemistry.

In another example, Cui *et al*. reported CPNs formed by coordination of Dy^{3+} ions with a vinylimidazole(Vin)-based polymer acting as a coordinating ligand [182]. The self-assembly was drive by the strong coordination interactions between imidazole rings and ester groups with Dy^{3+} ions. The NPs were further coated with silica stabilising them against disassembling in aqueous media. As a proof-of-concept, the NPs were internalised in fibroblast L929 and monitored in the cytoplasm by CLSM. Qualitatively, the CPNs showed predominant T_{2W} contrast, demonstrating the potential use of such NPs as multiscale cellular probes for both fluorescence imaging and MRI. However, no quantitative r_1 and r_2 measurements were reported. Along with this, Wang *et al*. developed CPNs using Gd^{3+} and $Ru(bpy)_3^{2+}$ [183]. These CPNs were endowed with red fluorescence and high MRI, which allowed differentiation of tumours from other tissues. The CPNs were synthesised via hydrothermal treatment producing spherical NPs with average diameter of 138 nm, as shown by SEM. The r_1 of the CPNs (29.30 $mM^{-1}s^{-1)}$ was six times larger than that of Gd-DTPA (4.95 $mM^{-1}s^{-1}$, tested under the same conditions). The r_2 value under the same experimental conditions was 22.67 $mM^{-1}s^{-1}$, with an r_2/r_1 ratio of 0.77. The imaging efficacy and the low toxicity were corroborated using HepG2 cells, zebrafish, and tumour-bearing mice as models. Finally,

in 2020, Sun *et al.* reported the formation of Gd^{3+}-Rose Bengal (RB) CPNs [184]. The CPNs were synthesised by solvothermal method using RB (as a photosensitiser) and Gd^{3+} ions (as metal nodes). The reaction yielded the formation of ultrasmall NPs with average size of 3.3 ± 0.8 nm, as shown by TEM. Interestingly, developed CPNs showed an enhanced fluorescence when compared with free RB. Moreover, the presence of Gd^{3+} ions allowed for the detection of MR signal, showing a strong T_{1w}-mediated CA with r_1 = 9.6 $mM^{-1}s^{-1}$. Finally, imaging performance was evaluated *in vivo* by i.v. injection of the CPNs in 4T1-tumour-bearing mice. The *in vivo* results showed both MRI and fluorescence imaging with excellent performance.

MRI/CT + PAI

Three examples of CPNs with both MRI and PAI contrast have been recently described. In 2015, An *et al*. prepared a core-shell structure made of a Fe_3O_4 nanocluster core bearing a carbocyanine-Gd^{3+} CPN as the outer shell [185]. The formed organic/inorganic hybrid exhibited a narrow size distribution centred at 75 nm. The use of performed Fe_3O_4-Carbon platforms, it was possible to fine tune the deposition of CPNs, resulting in an outer shell on the carbon layer. Interestingly, the final structure presented a high T_2 contrast effect with an r_2 = 224.5 $mM^{-1}s^{-1}$, which depends on the concentration and size of the iron oxide NPs (best results for 75 nm). The presence of Gd^{3+} ions in the shell conferred low T_1 response (r_1 = 0.5 $mM^{-1}s^{-1}$), and the cyanine-based ligand induced the generation of photoacoustic signals. The imaging efficiency was validated by *in vivo* experiments upon the accumulation of imaging probes on the targeted tumour. The use of cyanine-based ligands for the generation of PA signals was also used by Hu *et al*. for the preparation of ICG-loaded PDA-Fe^{3+} NPs [186]. First of all, PDA NPs were synthesised through a self-polymerization of dopamine in alkaline media. Then, Fe^{3+} ions were chelated via coordination interactions with catechol groups and ICG molecules were absorbed via π-π/electrostatic interactions. DLS measurements revealed an hD of 167 ± 3 nm with high stability after PEGylation process. On the one hand, the presence of ICG molecules conveniently improve the NIR optical absorption of PDA and decrease their fluorescence, which can enhance the PA contrast capability. On the other hand, Fe^{3+} ions induced a T_1 MRI contrast effect with an r_1 = 14.0 $mM^{-1}s^{-1}$. In addition, T_2 was evaluated exhibiting high contrast effect with r_2 = 83.3 $mM^{-1}s^{-1}$. Interestingly, remarkable therapeutic efficiency with minimal side effects was accomplished in a mouse 4T1 breast tumour after dual PAI/MRI imaging and PTT

treatments using low laser densities. In a similar example, Chen *et al*. prepared a DMCA nanocomplex based on Fe^{3+}–PDA with a transversal relaxivity high enough (r_2 = 45.92 $mM^{-1}s^{-1}$) to allow for dual-mode MRI imaging (r_2/r_1 = 6.11) [123]. In addition, the same CNPs loaded with DOX facilitate NIR-responsive on-demand and destroy the tumour directly by heat.

In a further step, Yang *et al*. described a general methodology to synthesise PEGylated CPNs showing fibber-like morphology through a phase–transfer reaction [187]. The CPNs were prepared by mixing diverse types of metal ions (e.g. Mn^{2+}, Ca^{2+}, Co^{2+}) and the cyanine-based ligand (ICG) together with poly–L–His-PEG (pHis–PEG) as a stabilising agent (**Figure 11**). The CPNs were produced through a facile phase-transfer reaction yielding fibber-like nanostructures with lengths at hundreds of nm as shown by TEM. Due to the specific intense NIR absorbance of Mn-ICG@pHis-PEG, the CPNs showed a sharp *in vivo* PAI contrast in 4T1-tumour-bearing mice, with signals that gradually increase in a time-dependent manner (**Figure 11d**). On top of that, the presence of Mn^{2+} ions allowed for concentration-dependent brightening effect under T_1 MRI, with an r_1 of 8.20 $mM^{-1}s^{-1}$, reasonably larger than that of free $MnCl_2$ (4.42 $mM^{-1}s^{-1}$) and the commercially available Gd-based T_1 contrast Magnevist®. Interestingly, the *in vivo* MRI imaging in mice bearing 4T1 tumours under a clinic 3T MR scanner showed T_{1W} signals brightened up in the tumour over time.

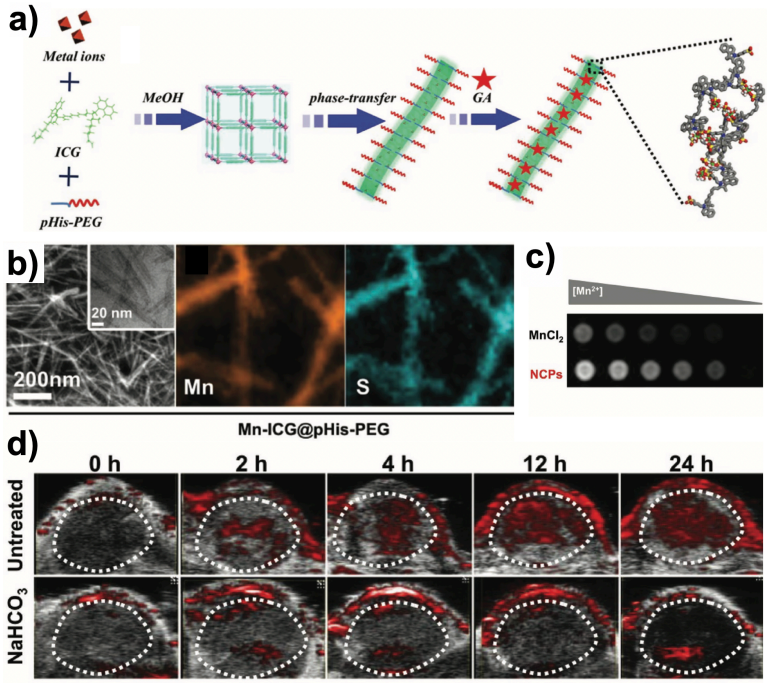

Figure 11. (a) One-step reaction of 1D PEGylated CPNs. (b) High-angle annular dark-field scanning transmission electron microscopy (HAADF-STEM) image and amplified TEM image inset; STEM-mapping for Mn and S. (c) T_{1w} MR images of $MnCl_2$ and Mn-ICG@pHis-PEG solutions with different concentrations of Mn^{2+}. (d) i.v. injection of Mn-ICG@pHis-PEG and PA images of the tumours at various time points. Adapted with permission from ref. [187], Copyright 2017 Wiley.

Yang *et al*. described the preparation of core-shell CPNs for dual MRI/PAI [188]. For this, CPNs containing Mn^{2+} ions (MRI) and IR825 (high NIR absorbance) were first prepared in a mixed solvent of DMF/methanol thorugh post-synthetic cation echange method. Then, the CPNs were combined with Hf^{4+} (a high-Z element with good CT signal and radiosensitisation capability) to furnish core-shell Mn-Hf-IR825 systems. The resulting NPs were coated with PDA and PEGylated, exhibiting spherical morphology with average hD about 110 nm. Accordingly, the presence of Mn^{2+} offers a brightening effect as a T_1 CA with an r_1 = 7.28 $mM^{-1}s^{-1}$, which is larger than the commercial CAs based on Gd and Mn. Interestingly, the CPNs were i.v. injected showing efficient tumour-homing ability, as noticed by MRI and PAI with low toxicity. Moreover, the CPNs accomplished high tumour killing efficacy by *in vivo* photothermal and synergistic radiation therapy in mouse tumour model experiments. More recently, in 2020, Tian *et al.* described the formation polyphenol-based CPNs through the reaction between ellagic acid and $Fe^{2+/3+}$ ions [189]. The CPNs were prepared via one-pot method used in their previous work, where albumin was employed as surfactant to control the formation and size of Fe-based CPN as CA for MRI [116]. The size of the

resulting CPNs was determined by TEM, showing uniform particle size with average diameter about 24 nm. Both relaxivity parameters were measured, showing a T_{1w}-mediated MRI contrast (r_1 = 2.54 and r_2 = 3.1 $mM^{-1}s^{-1}$). When compared with its previous system (GA-Fe@BSA), the r_2/r_1 was slightly increased (1.22). This increase was attributed to the larger molecular structure of ellagic acid when compared with GA. This different molecular structure between both ligands was beneficial for slowing down the molecular spin. Consequently, this speed reduction allowed for the increase of the spin correlation time after coordination with Fe ions. Finally, PAI measurements showed increased signal intensity 8.9-fold higher when compared with water.

MRI/CT + PAI + RI

The combination of MRI and PET techniques in a single nanoplatform offers an effective tool for the highly accurate diagnosis of several diseases, organism disorders and metabolism alterations. Their combination together with PAI imaging in a single CPN platform was described by Jin *et al*. in 2017 [190]. The authors reported the synthesis of ultra-small iron-GA CPNs (Fe-Ga CPNs) and the post-synthetic incorporation of ^{64}Cu as radiotracer. This approach represented a good strategy for the preparation of CPNs in one-step chelator-free methodology (**Figure 12**). The ultra-small NPs obtained (~ 5 nm, as shown by TEM images) where further functionalised with PEG allowing tumour accumulation with high labelling yield. Nevertheless, the quantitative determination of relaxivity parameters highlighted that these CPNs could act as moderate T_1 CA because of their low longitudinal relaxivity (r_1 = 3.50 $mM^{-1}s^{-1}$). This fact was compensated with a low transversal relaxivity value (r_2 = 0.97 $mM^{-1}s^{-1}$) that decreased the r_2/r_1 ratio, conferring a T_{1W}-dominated CA. The PAI was validated by the *in vivo* imaging upon injection, with highly efficient photothermal destruction upon NIR laser irradiation of the tumours, without harmful accumulation in vital organs.

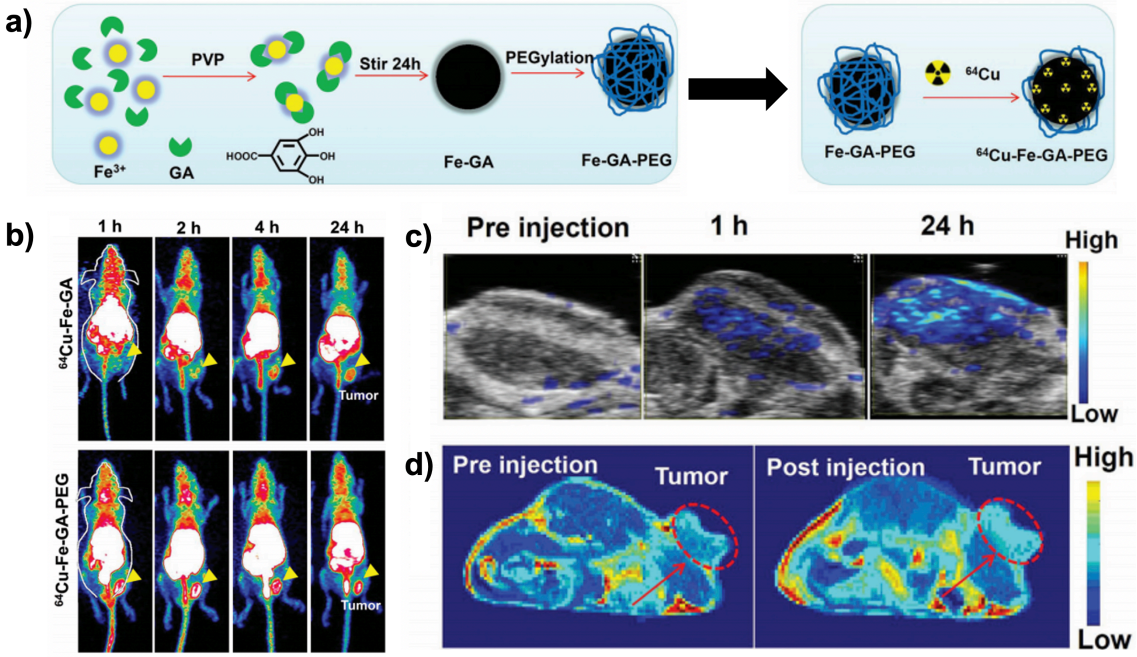

Figure 12. (a) Fe-Ga CPN preparation and PEGylation followed by ^{64}Cu labelling on Fe-GA-PEG CPNs through a chelator-free manner. (b) *In vivo* PET images of 4T1 tumour-bearing mice obtained at various time points (1, 2, 4, and 24 h) post i.v. of ^{64}Cu-Fe-GA CPNs without (upper) or with PEG (bottom) coating. The yellow triangle symbol represented the tumour site. (c) *In vivo* PA images of tumours on mice after injection with Fe-GA-PEG CPNs obtained at various time points (0 h, 1 h, and 24 h). (d) T_{1w} MRI of mice before and 24 h after i.v. injection with Fe-GA-PEG CPNs. Adapted with permission from ref. [190], Copyright 2017 Royal Society of Chemistry.

OI + PAI

In a single example, Chu *et al*. achieved a fluorescence/ PAI-guided combination photo/gene therapy using nanoformulations made of a Zn^{2+}-dipicolylamine (DPA) loading ICG and therapeutic genes [191]. The interaction between Zn^{2+} ions and sulfonate anions present in ICG molecules allowed for the assembly of CPNs with average diameter of 120 nm as shown by TEM images. The CPNs (with λ_{ex} = 808 nm) exhibited an enhanced PA signal compared to ICG. In a 4T1 xenograft mouse model, PTT combined with gene therapy, completely eliminated the tumours in animals without significant side effects. Most remarkably, *in vivo* results did not show tumour relapsing after three weeks.

4. Perspectives

Researchers continue to pursue the idea of developing multiplatform systems that allow their use in a wide range of diagnostic techniques. The main advantage is to provide in a single platform all the necessary elements without the need to change the corresponding imaging agent. Nanostructuration and predesigned formulation could substantially improve the formation of multifunctional systems with outstanding properties. With these advances, the expected benefits are numerous due to the highly sensitive diagnostic capacity, hand in hand with personalised Medicine to the patient and prioritising early diagnosis. In this sense, CPNs exhibit great prospective as CAs and bioimaging probes thanks to the combination of the inherent advantages demonstrated by nanostructured materials (high surface area, colloidal stability, cell internalisation and controlled release, among others). Specially, the richness and versatility offered by coordination chemistry, allows for the development of nanostructured functional materials with high potential for its clinical transfer. Though the number of metal ions that can be used for their preparation is considerable, there is a preferential use of some metal ions as dictated by the specific requirements of each technique. For instance, Gd^{3+}, Mn^{2+} and $Fe^{2+/3+}$ are preferably used for MRI, lanthanides in the case of OI and other metal ions such as Hf^{4+} for CT or $^{64}Cu^{2+}$ or ^{99m}Tc for PET and SPECT, respectively. This can also be extrapolated to the use of ligands; although the range of possibilities is extensive, some of them concentrate more attention such as polyphenol ligands, cyanine or $Ru(bpy)_3^{2+}$ that confer added value to the NP such as chemotherapy or fluorescence activity, among others. A schematic compilation of the most successful combination of metal ion and functional ligands reviewed in this manuscript is shown in **Table 3**. Overall, the fine-tuning selection of ligands and metals provides a great scope for the application of CPNs in a multiplatform imaging system.

Going deeper into detail on the different techniques, it becomes more evident the specific needs and evolution for each one of them. For instance, trends followed by researchers over the last years in MRI are mainly heading towards the development of novel NPs that minimise the toxicity of metal ions such as Gd^{3+}, Mn^{2+} and/or the progressive development of T_1/T_2 DMCAs (**Table 2**). Concerning OI, it has already been demonstrated that by adjusting the ratio of the metals (or even ligands) the resulting luminescence can be easily tuned, allowing to perform multiple logic operations which can be interesting for their use in biological systems. Nevertheless, the

absorption and quantum yields must be optimised before clinical applications. In the case of RI, future tendencies go to the use of chelator-free systems, avoiding the laborious synthesis procedures with extreme conditions and the reduction of the side effects. However, limited number of examples has been so far described in most of these areas so further work will be required before any general trend and/or conclusions can be extracted. This is even more applicable for techniques such as CT or PAI, where only a few examples have been reported. Finally, a trending tendency is the combination of different imaging techniques within a single platform to reduce ambiguities and false positives or errors caused by undetected organism alterations. A compilation of the few examples so far described in this area is summarised in **Table 4**. Additionally, the demonstrated versatility of CPNs make feasible to develop these kind of nanosystems for emerging imaging modalities. In this novel techniques, such as second NIR (NIR-II) imaging [192,193], afterglow imaging [194,195] and chemiluminescence imaging [196,197], the use of molecular probes to increase the signal-to-noise ratios and penetration depth is crucial.

The other great battleground in the future for CPNs is the translation into hospitals and applied medical research. Researchers have to face the current challenges in order to provide more evidence of the effectiveness of CPNs in terms of stability, biocompatibility and biodegradability in real biological environments. Development of proper pharmacokinetic profiles will be another major step. If successful, CPNs performing efficiently both detection and therapy settle a new basis for a novel generation of personalised therapy. In this sense, previous *in vivo* studies so far reported with animal models are encouraging in terms of biocompatibility, biostability and imaging performing. These studies revealed that nanostructuration might attenuate the toxic effects of some of the metal ions while the formation of protective shells based on polymers (e.g. PEG), has demonstrated its effectiveness to improve the stability. On top of that, protective coatings (e.g. PDA) can be functionalised with active targeting ligands to enhance accumulation in tumours.

To conclude, there are two other areas we do consider deserve special attention in the near future. The first one is the development of several novel fundamental studies that help to decipher the critical role played by the ligands, coordination sphere, surface-to-volume ratios and the accessibility of water molecules within the NPs. We should not forget that most of the times, these NPs are obtained under strict out-of-equilibrium

conditions lacking, therefore, a well-defined chemical structure. In other words, future work is needed to assess a proper structure-property correlation. Secondly, we do aim our colleagues to collect all the knowledge so far gained in this area and summarised in this review to target more specific applications and medical challenges where CPNs can bring added value.

Table 1. Summary of r_1 and r_2 relaxivities for commercial contrast agents.

Brand name	Metal	Formula	r_1 ($mM^{-1}s^{-1}$)	r_2 ($mM^{-1}s^{-1}$)	r_2/r_1	Magnetic field (T)	Ref.
Magnevist®	Gd^{3+}	Gd-DTPA	4.1	4.6	1.12		
MultiHance®	Gd^{3+}	Gd-BOPTA	6.3	8.7	1.38		
Omniscan™	Gd^{3+}	Gd-DTPA-BMA	4.3	5.2	1.21		
Dotarem®/Clariscan ®	Gd^{3+}	Gd-DOTA	3.6	4.3	1.19		[198]
ProHance®	Gd^{3+}	Gd-HP-DO3A	4.1	5.0	1.22	1.5	
Gadavist®	Gd^{3+}	Gd-BT-DO3A	5.2	6.1	1.17		
Eovist®/Primovist®	Gd^{3+}	Gd-EOB-DTPA	6.9	8.7	1.26		
Teslascan®	Mn^{2+}	Mn-DPDP	3.1	2.3	0.74		
Lumenhance®	Mn^{2+}	$MnCl_2$	8.0	6.0	0.75		
Resovist®	Fe^{2+}/Fe^{3+}	Fe_2O_3 (SPIONs)	25.4	151.0	5.94	0.5	[199]
Endorem®	Fe^{2+}/Fe^{3+}	Fe_2O_3 (SPIONs)	40.0	160.0	4.00	0.5	
Sinerem®	Fe^{2+}/Fe^{3+}	Fe_2O_3 (SPIONs)	25.0	160.0	6.40	0.5	

Table 2. Summary of r_1 and r_2 relaxivities for reported CPN-based contrast agents.

System	Metal	r_1 ($mM^{-1}s^{-1}$)	r_2 ($mM^{-1}s^{-1}$)	r_2/r_1	Magnetic field (T)	Ref.
Gd-NCP	Gd^{3+}	6.58 (pH=5.5) 0.18 (pH=7.4)	-	-	3.0	[96]
$Gd^{3+}/[Fe(CN)_6]^{3-}$	Gd^{3+}	11.40	12.60	1.01	4.7	[98]
Gd-Micelles	Gd^{3+}	34.12	20.16	0.59	3.0	[99]
Gd-TA	Gd^{3+}	25.5	30.3	1.19	1.0	[100]
f -CPPs@PVP	Gd^{3+}	8.0	10.8	1.35	0.5	[179]
Ir-Gd-CPP	Gd^{3+}	29.5	-	-	3.0	[180]
Gd/Yb-Ru PEG@NCPs	Gd^{3+}	26.27	-	-	1.2	[181]
Gd-Ru NCPs	Gd^{3+}	29.30	22.67	0.77	1.2	[183]
$FcGd@SiO_2$(SBITC)-RGD	Gd^{3+}	5.10	21.7	4.25	3.0	[122]
Gd-RB	Gd^{3+}	9.6	-	-	9.4	[184]
MSN-Gd	Mn^{2+}	28.80 10.20	65.50 110.8	2.27 10.86	3.0 9.4	[94]
Mn-NCP-PEG-AA	Mn^{2+}	7.60	70.30	9.25	3.0	[106]
Mn-IR825@PDA-PEG	Mn^{2+}	7.48	-	-	3.0	[107]
Mn-SS	Mn^{2+}	9.95	-	-	3.0	[108]
FMCNP	Mn^{2+}	6.46	-	-	7.0	[109]
Mn^{2+}-PNP	Mn^{2+}	17.35	37.99	2.19	4.7	110]
MTX-Mn@PEG	Mn^{2+}	7.76	-	-	0.5	[111]
BM@NCP(DSP)-PEG	Mn^{2+}	9.23 (pH=6.5) 1.75 (pH=7.4)	-	-	3.0	[72]
Mn-ICG@pHis-PEG	Mn^{2+}	4.42	-	-	3.0	[187]
NMOP-PEG	Mn^{2+}	7.28	-	-	3.0	[188]
GA-Fe@BSA	Fe^{3+}	0.89	0.95	1.07	0.5	[116]
EA-Fe@BSA	Fe^{3+}	2.54	3.1	1.22	0.5	[189]
Fe-GA@PEG-PLGA	Fe^{3+}	10.46	-	-	7.0	[119]
Fe-mPEG-S-Trityl-Cys-Dopa	Fe^{3+}	1.53	-	-	1.2	[120]
$PDAs@CP_3$	Fe^{3+}	7.52	45.92	6.11	1.5	[123]
SPION@CPP-Fe	Fe^{3+}	2.80	185.3	66.2	7.0	[124]
Fe-NCP	Fe^{3+}	5.30	10.90	2.06	7.0	[125]
catAZT-NCP	Fe^{3+}	0.15	117.5	783.3	7.0	[82]
PDA-Fe^{3+}-ICG	Fe^{3+}	14.0	83.3	5.95	3.0	[186]
Fe-GA-PEG	Fe^{3+}	3.50	0.97	0.28	1.0	[190]
Gd-Fe-TA CPNs	Gd^{3+}/Fe^{3+}	9.30	11.72	1.26	1.0	[120]
Fe_3O_4@C@Cy-Gd^{3+}	Gd^{3+}/Fe^{3+}	0.5	224.5	449	3.0	[182]

Table 3. CPNs for Bioimaging

Imaging Technique	Mode	Metal	Ligand	*In vitro*	*In vivo*
MRI	T_1	Gd^{3+}, Mn^{2+}	NH_2-BDC, cyano-bridged, Asp, bisphosphonate, BDC, BTC, IR825, DTA, Fmoc, Met, DSP	[96] [106] [111]	[72] [94] [98] [99] [100] [107] [108] [109] [111] [116] [117] [120] [121]
		$Fe^{2+/3+}$	GA, PDA, TA		
	T_2	$Fe^{2+/3+}$	dhc, bix	[82]	
	T_1/T_2	$Fe^{2+/3+}$, $Fe^{2+/3+}/Gd^{3+}$, SPIONs	DCFe, PDA, dhc, bix	[124]	[122] [123] [125]
CT	-	I^+, Hf^{4+}	I_4–BDC–H_2, BATA		[128]
OI	CPNs-QDs	Zn^{2+}, Tb^{3+}, Eu^{3+}	K-PTC, BTB, DDM, hPA	[137]	
	Photoluminiscence	Zn^{2+},Tb^{3+}, Eu^{3+}, Ce^{3+}, Zr^{4+}, Cu^+	TCPP, $Ru(bpy)_3^{2+}$, polytriazole	[142]	[140]
	Encapsulation of dyes (ICG, Cur, $CurBF_2$, ANF, rhod B, Ce6, FITC, PBH, A568, DiR)	Ca^{2+},Co^{2+}, Zn^{2+}, Gd^{3+}, Hf^{4+}, Cu^{2+}, Zr^{4+}	SDS, HEPES, dhc, bix, bisphosphonate, His	[45] [143] [145]	[62] [64] [71] [144] [146]
RI	PET	^{64}Cu, W^{4+}	GA, phthalocyanine	[157]	[156]
	SPECT	^{99m}Tc, Ca^{2+}, Hf^{4+}	Porphyrin, TCPP		[159]
PAI	-	Fe^{3+}	PC, DB, PG, GA, EG, TA	[178]	

Table 4. CPNs for Bi- and Trimodal Imaging

Imaging Technique	Mode	Metal	Ligand	*In vitro*	*In vivo*
MRI/CT + OI	T_1 + Phospohorescence	Gd^{3+}, Ir^{3+}	BDA	[179] [180]	
	T_1 + Fluorescence	Gd^{3+}, Yb^{3+}	$Ru(bpy)_3^{2+}$, RB		[181] [183] [184]
	T_2 + Fluorescence	Dy^{3+}	Vyn	[182]	
MRI/CT + PAI	T_1 and/or T_2 + PA	Gd^{3+}, $Fe^{2+/3+}$, Mn^{2+}, Ca^{2+},Co^{2+}, Hf^{4+}	Cyanine-based, ICG, PDA, IR825, EA		[185] [186] [187] [188] [189]
MRI/CT + PAI + RI	T_1 + PA + PET	$Fe^{2+/3+}$, ^{64}Cu	GA		[190]
OI + PAI	Fluorescence + PA	Zn^{2+}	ICG, DPA		[191]

Acknowledgments

This work was supported by grants RTI2018-098027-B-C21 and CTQ2016-75363-R from the Spanish Government funds and by the European Regional Development Fund (ERDF). The ICN2 is funded by the CERCA programme / Generalitat de Catalunya. The ICN2 is supported by the Severo Ochoa Centres of Excellence programme, funded by the Spanish Research Agency (AEI, grant no. SEV-2017-0706). R. S. thanks the Ministerio de Educación, Cultura y Deporte for the predoctoral grant FPU14/ 03170. S.S.-G. acknowledges the support from MINECO BES-2015-071492 grant.

References

[1] X. Han, K. Xu, O. Taratula, K. Farsad, Applications of Nanoparticles in Biomedical Imaging, Nanoscale 11 (2019) 799–819.

[2] X. Li, Z. Cai, L.-P. Jiang, Z. He, J.-J. Zhu, Metal-Ligand Coordination Nanomaterials for Biomedical Imaging, Bioconjug. Chem. 31 (2020) 332–339.

[3] J. Fang, H. Nakamura, H. Maeda, The EPR Effect: Unique Features of Tumor Blood Vessels for Drug Delivery, Factors Involved, and Limitations and Augmentation of the Effect, Adv. Drug Deliv. Rev. 63 (2011) 136–151.

[4] H. Xing, K. Hwang, Y. Lu, Recent Developments of Liposomes as Nanocarriers for Theranostic Applications, Theranostics 6 (2016) 1336–1352.

[5] Ö.M.Ö. Öztürk, B. Garipcan, F. Inci, Biomedical Applications: Liposomes and Supported Lipid Bilayers for Diagnostics, Theranostics, Imaging, Vaccine Formulation, and Tissue Engineering in: F. Kök, Y. A. Arslan, F. Inci (Eds), Biomimetic Lipid Membranes: Fundamentals, Applications, and Commercialization. Springer, Cham, 2019, pp 193-212.

[6] M. Silindir-Gunay, A. Y. Ozer, Liposomes and micelles as nanocarriers for diagnostic and imaging purposes in: A. M. Grumezescu. (Eds.), Design of Nanostructures for Theranostics Applications, William Andrew Publishing, 2018, pp 305–340.

[7] C. F. Chiu, W. A. Saidi, V. E. Kagan, A. Star, Defect-Induced Near-Infrared Photoluminescence of Single-Walled Carbon Nanotubes Treated with Polyunsaturated Fatty Acids, J. Am. Chem. Soc. 139 (2017) 4859–4865.

[8] Z. Sheng, L. Song, J. Zheng, D. Hu, M. He, M. Zheng, G. Gao, P. Gong, P. Zhang, Y. Ma, L. Cai, Protein-Assisted Fabrication of Nano-Reduced Graphene Oxide for Combined In Vivo Photoacoustic Imaging and Photothermal Therapy, Biomaterials 34 (2013) 5236–5243.

[9] E.C. Cho, C. Glaus, J. Chen, M.J. Welch,Y. Xia, Inorganic nanoparticle–based contrast agents for molecular imaging. Trends Mol. Med. 16 (2010) 561–573.

[10] K. Cherukula, K.M. Lekshmi, S. Uthaman, K. Cho, C.-S. Cho, I.-K. Park, Multifunctional Inorganic Nanoparticles: Recent Progress in Thermal Therapy and Imaging, Nanomaterials 6 (2016) 76.

[11] D. Kim, J. Kim, Y.I. Park, N. Lee, T. Hyeon, Recent Development of Inorganic Nanoparticles for Biomedical Imaging, ACS Cent. Sci. 4 (2018) 324–336.

[12] O. T. Bruns, T. S. Bischof, D. K. Harris, D. Franke, Y. Shi, L. Riedemann, A. Bartelt, F. B. Jaworski, J. A. Carr, C. J. Rowlands, Next-Generation In Vivo Optical Imaging with Short-Wave Infrared Quantum Dots, Nat. Biomed. Eng. 1 (2017) 0056.

[13] A. Burns, H. Ow, U. Wiesner, Fluorescent Core–Shell Silica Nanoparticles: Towards "Lab on a Particle" Architectures for Nanobiotechnology, Chem. Soc. Rev. 35 (2006) 1028–1042.

[14] S. Wang, Y. Chen, X. Li, W. Gao, L. Zhang, J. Liu, Y. Zheng, H. Chen, J. Shi, Injectable 2D MoS2 -Integrated Drug Delivering Implant for Highly Efficient NIR-Triggered Synergistic Tumor Hyperthermia, Adv. Mater. 27 (2015) 7117–7122.

[15] L. Rao, L. L. Bu, B. Cai, J. H. Xu, A. Li, W. F. Zhang, Z. J. Sun, S. S. Guo, W. Liu and T. H. Wang, Cancer Cell Membrane-Coated Upconversion Nanoprobes for Highly Specific Tumor Imaging, Adv. Mater. 28 (2016) 3460–3466.

[16] J. Song, X. Yang, Z. Yang, L. Lin, Y. Liu, Z. Zhou, Z. Shen, G. Yu, Y. Dai and O. Jacobson, Rational Design of Branched Nanoporous Gold Nanoshells with Enhanced Physico-Optical Properties for Optical Imaging and Cancer Therapy, ACS Nano 11 (2017) 6102–6113.

[17] Y. Jiang, K. Pu, Multimodal Biophotonics of Semiconducting Polymer Nanoparticles, Acc. Chem. Res. 51 (2018) 1840−1849.

[18] J. Li, K. Pu, Development of Organic Semiconducting Materials for Deep-Tissue Optical Imaging, Phototherapy and Photoactivation, Chem. Soc. Rev. 48 (2019) 38-71.

[19] J. Li, K. Pu, Semiconducting Polymer Nanomaterials as Near-Infrared Photoactivatable Protherapeutics for Cancer, Acc. Chem. Res. 53 (2020) 752−762.

[20] M. L. Hans, A.M. Lowman, Biodegradable Nanoparticles for Drug Delivery and Targeting, Curr. Opin. Solid St. M. 6 (2002) 319–327.

[21] S. Kitagawa, R. Kitaura, S. Noro, Functional Porous Coordination Polymers, Angew. Chem. Int. Ed. 43 (2004) 2334–2375.

[22] L.J. Chen, H.B. Yang, Construction of Stimuli-Responsive Functional Materials via Hierarchical Self-Assembly Involving Coordination Interactions, Acc. Chem. Res. 51 (2018) 2699–2710.

[23] G. Lan, K. Ni, W. Lin, Nanoscale Metal-organic Frameworks for Phototherapy of Cancer, Coord. Chem. Rev. 379 (2019) 65–81.

[24] K. Lu, T. Aung, N. Guo, R. Weichselbaum, W. Lin, Nanoscale Metal-Organic Frameworks for Therapeutic, Imaging, and Sensing Applications, Adv. Mater. 30 (2018) 1–20.

[25] F. Novio, J. Simmchen, N. Vázquez–Mera, L. Amorín-Ferré, D. Ruiz-Molina, Coordination Polymer Nanoparticles in Medicine, Coord. Chem. Rev. 257 (2013) 2839–2847.

[26] W. Lin, W.J. Rieter, K.M.L. Taylor, Modular Synthesis of Functional Nanoscale Coordination Polymers, Angew. Chem. Int. Ed. 48 (2009) 650–658.

[27] A. M Spokoyny, D. Kim, A. Sumrein, C. A Mirkin, Infinite Coordination Polymer Nano- and Microparticle Structures, Chem. Soc. Rev. 38 (2009) 1218–1227.

[28] H. J. Lee, Y. J. Cho, W. Cho, M. Oh, Controlled Isotropic or Anisotropic Nanoscale Growth of Coordination Polymers: Formation of Hybrid Coordination Polymer Particles, ACS Nano 7 (2013) 491–499.

[29] M. Oh, C.A. Mirkin, Chemically Tailorable Colloidal Particles from Infinite Coordination Polymers, Nature 438 (2005) 651–654.

[30] X. Sun, S. Dong, E. Wang, Coordination–Induced Formation of Submicrometer-Scale, Monodisperse, Spherical Colloids of Organic-Inorganic Hybrid Materials at Room Temperature, J. Am. Chem. Soc. 127 (2005) 13102–13103.

[31] N. N. Adarsh, F. Novio, D. Ruiz-Molina, Coordination Polymers Built from 1,4–Bis(Imidazol–1–Ylmethyl)Benzene: From Crystalline to Amorphous, Dalt. Trans. 45 (2016) 11233–11255.

[32] I. Imaz, D. Maspoch, C. Rodríguez-Blanco, J.M. Pérez-Falcón, J. Campo, D. Ruiz-Molina, Angew. Chem. Int. Ed. 47 (2008) 1857–1860.

[33] M. Guardingo, F. Busqué, D. Ruiz-Molina, Reactions in Ultra–Small Droplets by Tip–Assisted Chemistry, Chem. Commun. 52 (2016) 11617–11626.

[34] M. Guardingo, P. González-Monje, F. Novio, E. Bellido, F. Busqué, G. Molnár, A. Bousseksou, D. Ruiz-Molina, Synthesis of Nanoscale Coordination Polymers in Femtoliter Reactors on Surfaces, ACS Nano 10 (2016), 3206–3213.

[35] E. Bellido, P. González-Monje, M. Guardingo, F. Novio, A. Sánchez, M. Montero, G. Molnar, A. Bousseksou, D. Ruiz-Molina, Nanoscale Coordination Polymers Obtained in Ultrasmall Liquid Droplets on Solid Surfaces and Its Comparison to Different Synthetic Volume Scales, RSC Adv. 6 (2016) 76666–76672.

[36] A. Bousseksou, G. Molnár, L. Salmon, W. Nicolazzi, Molecular Spin Crossover Phenomenon: Recent Achievements and Prospects, Chem. Soc. Rev. 40 (2011) 3313–3335.

[37] J. Puigmartí–Luis, Microfluidic Platforms: A Mainstream Technology for the Preparation of Crystals, Chem. Soc. Rev. 43 (2014) 2253–2271.

[38] a) Z.-Y. Xiao, X. Zhao, X.-K. Jian, Z.-T. Li, Tunable Coordinative Assembly of a Disc-Like Molecule and Metal Ions: From Mirospheres to Microtubes and Microrods, Chem. Mater. 23 (2011) 1505–1511; b) Y.-M. Jeon, G. S. Armatas, D. Kim, M. G. Kanatzidis, C. A. Mirkin, Tröger's-Base-Derived Infinite Coordination Polymer Microparticles, Small 5 (2009) 46–50.

[39] J. Huo, L. Wang, E. Irran, H. Yu, J. Gao, D. Fan, B. Li, J. Wang, W. Ding, A. M. Amin, C. Li, L. Ma, Hollow Ferrocenyl Coordination Polymer Microspheres with Micropores in Shells Prepared by Ostwal Ripening, Angew. Chem. Int. Ed. 49 (2010) 9237–9241.

[40] Y.-M. Jeon, J. Heo, C. A. Mirkin, Dynamic Interconversion of Amorphous Microparticles and Crystalline Rods in Salen-Based Homochiral Infinite Coordination Polymers, J. Am. Chem. Soc. 129 (2007) 7480-7481.

[41] Y. Liu, F. Boey, L. Lisa Lao, H. Zhang, X. Liu, Q. Zhang, Postchemistry of Inorganic–Organic Hybrid Particles in Aqueous Solution: Metal-Cation Exchange, Chem. Asian J. 6 (2011) 1004–1006.

[42] M. Oh, C. A. Mirkin, Ion Exchange as a Way of Controlling the Chemical Compositions of Nano- and Microparticles Made from Infinite Coordination Polymers, Angew. Chem. Int. Ed. 45 (2006) 5492–5494.

[43] S. M. Cohen, Postsynthetic Methods for the Functionalization of Metal-Organic Frameworks, Chem. Rev. 112 (2012) 970–1000.

[44] K.M.L. Taylor-Pashow, J, Della Rocca, Z. Xie, S. Tran, W. Lin, Postsynthetic Modifications of Iron-Carboxylate Nanoscale Metal-Organic Frameworks for Imaging and Drug Delivery, J. Am. Chem. Soc. 131 (2009) 14261–14263.

[45] F. Novio, J Lorenzo, F. Nador, K Wnuk, D. Ruiz-Molina, Carboxyl Group (-CO_2H) Functionalized Coordination Polymer Nanoparticles as Efficient Platforms for Drug Delivery, Chem. Eur. J. 47 (2014) 15443–15450.

[46] F. Novio, D. Ruiz-Molina, Hydrophobic coordination polymer nanoparticles and application for oil–water separation, RSC Advances 4 (2014) 15293–15296.

[47] P. Gonzalez–Monje, F. Novio, D. Ruiz–Molina, Covalent Grafting of Coordination Polymers on Surfaces: The Case of Hybrid Valence Tautomeric Interphases, Chem. Eur. J. 21 (2015) 10094–10099.

[48] P.F. Gao, L.L. Zheng, L. J. Liang, X.X. Yang, Y.F. Li, C.Z. Huang, A New Type of pH-Responsive Coordination Polymer Sphere as a Vehicle for Targeted Anticancer Drug Delivery and Sustained Release, J. Mater. Chem. B 1 (2013) 3202–3208.

[49] L. Bai, F. Song, X.H. Wang, J.Y. Q. Cao, X. Han, X.L. Wang, Y.Z. Wang, Ligand-Metal-Drug Coordination Based Micelles for Efficient Intracellular Doxorubicin Delivery, RSC Adv. 5 (2015) 47629–47639.

[50] K. Han, W.Y. Zhang, J. Zhang, Z.Y. Ma, H.Y. Han, pH–Responsive Nanoscale Coordination Polymer for Efficient Drug Delivery and Real–Time Release Monitoring, Adv. Health Mater. 6 (2017) 1–9. https://doi.org/10.1002/adhm.201700470.

[51] S. Xu, J. Liu, D. Li, L. Wang, J. Guo, C. Wang, C Chen, Fe-Salphen Complexes from Intracellular pH-Triggered Degradation Of Fe3O4@Salphen-InIIICPPs for Selectively Killing Cancer Cells, Biomaterials 35 (2014) 1676–1685.

[52] T. Wang, X. Liu, Y. Zhu, Z.D. Cui, X.J. Yang, H. Pan, H. K.W.K. Yeung, S. Wu, Metal Ion Coordination Polymer-Capped pH-Triggered Drug Release System on Titania Nanotubes for Enhancing Self-Antibacterial Capability of Ti Implants, ACS Biomater. Sci. Eng. 3 (2017) 816–825.

[53] H. Ejima, J. J. Richardson, K. Liang, J. P. Best, M. P. Van Koeverden, G. K.Such, J. Cui, F. Caruso, One-Step Assembly of Coordination Complexes for Versatile Film and Particle Engineering, Science 341 (2013) 154–157.

[54] M. A. Rahim, H. Ejima, K. L. Cho, K. Kempe, M. Müllner, J. P. Best, F. Caruso, Coordination-Driven Multistep Assembly of Metal-Polyphenol Films and Capsules, Chem. Mater. 26 (2014) 1645–1653.

[55] Y. Ping, J. Guo, H. Ejima, X. Chen, J. J. Richardson, H. Sun, F. Caruso, pH-Responsive Capsules Engineered from Metal-Phenolic Networks for Anticancer Drug Delivery, Small 11 (2015) 2032–2036.

[56] Y. Ju, J. Cui, H. Sun, M. Müllner, Y. Dai, J. Guo, N. Bertleff-Zieschang, T. Suma, J.J. Richardson, F. Caruso, Engineered Metal-Phenolic Capsules Show Tunable Targeted Delivery to Cancer Cells, Biomacromolecules 17 (2016) 2268–2276.

[57] Y. Ju, Q. Dai, J. Cui, Y. Dai, T. Suma, J.J. Richardson, F. Caruso, Improving Targeting of Metal-Phenolic Capsules by the Presence of Protein Coronas, ACS Appl. Mater. Interfaces 8 (2016) 22914–22922.

[58] J. H. Park, K. Kim, J. Lee, J. Y. Choi, D. Hong, S. H. Yang, F. Caruso, Y. Lee, I. S. Choi, A Cytoprotective and Degradable Metal–Polyphenol Nanoshell for Single-Cell Encapsulation, Angew. Chem. Int. Ed. 53 (2014) 12420–12425.

[59] Q. A. Besford, Y. Ju, T. Y. Wang, G. Yun, P. V. Cherepanov, C. E. Hagemeyer, F. Cavalieri, F. Caruso, Self-Assembled Metal-Phenolic Networks on Emulsions as Low-Fouling and pH-Responsive Particles, Small 14 (2018), 1–9.

[60] W. Huang, P. Hao, J. Qin, S. Luo, T. Zhang, B. Peng, H. Chen, X. Zan, Hexahistidine-Metal Assemblies: A Promising Drug Delivery System, Acta Biomater. 90 (2019) 441–452.

[61] F. Nador, F. Novio, D. Ruiz-Molina, Coordination Polymer Particles with Ligand–Centred pH-Responses and Spin Transition, Chem. Commun. 50 (2014) 14570–14572.

[62] J. Liu, H. Wang, X. Yi, Y. Chao, Y. Geng, L. Xu, K. Yang, Z. Liu, pH-Sensitive Dissociable Nanoscale Coordination Polymers with Drug Loading for Synergistically Enhanced Chemoradiotherapy, Adv. Funct. Mater. 27 (2017) 1–10.

[63] J. Liu, L. Tian, R. Zhang, Z. Dong, H. Wang, Z. Liu, Collagenase-Encapsulated pH-Responsive Nanoscale Coordination Polymers for Tumor Microenvironment Modulation and Enhanced Photodynamic Nanomedicine, ACS Appl. Mater. Interfaces 10 (2018) 43493–43502.

[64] Y. Yang, L. Xu, W. Zhu, L. Feng, J. Liu, Q Chen, Z. Dong, J. Zhao, Z. Liu, M. Chen, One-Pot Synthesis of pH-Responsive Charge-Switchable PEGylated Nanoscale Coordination Polymers for Improved Cancer Therapy, Biomaterials 156 (2018) 121–133.

[65] B. Wang, M. Jacquet, K. Wang, K. Xiong, M. Yan, J. Courtois, G. Royal, pH-Induced Fragmentation of Colloids Based on Responsive Self-Assembled Copper(II) Metallopolymers, New J. Chem. 42 (2018) 7823–7829.

[66] P. V. Cherepanov, M. A. Rahim, N. Bertleff–Zieschang, M. A. Sayeed; A. P. O'Mullane, S. E. Moulton, F. Caruso, Electrochemical Behavior and Redox–Dependent Disassembly of Gallic Acid/FeIIIMetal-Phenolic Networks, ACS Appl. Mater. Interfaces 10 (2018) 5828–5834.

[67] S. Buwalda, B. Nottelet, A. Bethry, R. J Kok, N. Sijbrandi, J. Coudane, Reversibly Core–Crosslinked PEG–P(HPMA) Micelles: Platinum Coordination Chemistry for Competitive-Ligand-Regulated Drug Delivery, J. Colloid Interface Sci. 535 (2019) 505–515.

[68] Y. Zhang, Y. Guo, S. Wu, H. Liang, H. Xu, Photodegradable Coordination Polymer Particles for Light–Controlled Cargo Release, ACS Omega 2 (2017) 2536–2543.

[69] 69].J. Liu, G. Yang, W. Zhu, Z. Dong, Y. Yang, Y. Chao, Z. Liu, Light-Controlled Drug Release from Singlet-Oxygen Sensitive Nanoscale Coordination Polymers Enabling Cancer Combination Therapy, Biomaterials 146 (2017) 40–48.

[70] X. G. Hu, X. Li, S. I. Yang, Novel Photochromic Infinite Coordination Polymer Particles Derived from a Diarylethene Photoswitch, Chem. Commun. 51 (2015) 10636–10639.

[71] S. Li, Q. Zou, Y. Li, C. Yuan, R. Xing, X. Yan, Smart Peptide-Based Supramolecular Photodynamic Metallo–Nanodrugs Designed by Multicomponent Coordination Self-Assembly, J. Am. Chem. Soc. 140 (2018) 10794–10802.

[72] J. Liu, Q. Chen, W. Zhu, X. Yi, Y. Yang, Z. Dong, Z. Liu, Nanoscale-Coordination–Polymer–Shelled Manganese Dioxide Composite Nanoparticles: A Multistage Redox/pH/H_2O_2-Responsive Cancer Theranostic Nanoplatform, Adv. Funct. Mater. 27 (2017) 1605926.

[73] Y. Wang, Y. Wu, F. Li, D. Chen, Folic Acid-Modified Iridium(III) Coordination Polymeric Nanoparticles Facilitating Intracellular Release of a Phosphorescent Residue Capable of Nuclear Entry, Inorg. Chem. Commun. 40 (2014) 143–147.

[74] F. Pu, E. Ju, J. Ren, X. Qu, Multiconfigurable Logic Gates Based on Fluorescence Switching in Adaptive Coordination Polymer Nanoparticles, Adv. Mater. 26 (2014) 1111–1117.

[75] F. Pu, J. Ren, X. Qu, "Plug and Play" Logic Gates Based on Fluorescence Switching Regulated by Self-Assembly of Nucleotide and Lanthanide Ions, ACS Appl. Mater. Interfaces 6 (2014) 9557–9562.

[76] R.-R. Gao, S. Shi, Y.-J. Li, M. Wumaier, X.-C. Hu, T.-M. Yao, Coordination Polymer Nanoparticles from Nucleotide and Lanthanide Ions as a Versatile Platform for Color-Tunable Luminescence and Integrating Boolean Logic Operations, Nanoscale 9 (2017) 9589–9597.

[77] L. Bai, X.H. Wang, F. Song, X.L. Wang, Y.Z. Wang, "AND" Logic Gate Regulated pH and Reduction Dual–Responsive Prodrug Nanoparticles for Efficient Intracellular Anticancer Drug Delivery, Chem. Commun. 51 (2015) 93–96.

[78] L. Amorín-Ferré, F. Busqué, J.L. Bourdelande, D. Ruiz-Molina, J. Hernando, F. Novio, Encapsulation and Release Mechanisms in Coordination Polymer Nanoparticles, Chem. Eur. J. 19 (2013) 17508–17516.

[79] I. Imaz, J. Hernando, D. Ruiz-Molina, D. Maspoch, Metal-Organic Spheres as Functional Systems for Guest Encapsulation, Angew. Chem. Int. Ed. 48 (2009) 2325–2329.

[80] I. Imaz, M. Rubio-Martínez, L. García-Fernández, F. García, D. Ruiz-Molina, J. Hernando, V. Puntes, D. Maspoch, Coordination Polymer Particles as Potential Drug Delivery Systems, Chem. Commun. 46 (2010) 4737–4739.

[81] W. J. Rieter, K. M. Pott, K. M. L. Taylor, W. Lin, Nanoscale Coordination Polymers for Platinum–Based Anticancer Drug Delivery. J. Am. Chem. Soc. 130 (2008) 11584–11585.

[82] R. Solórzano, O. Tort, J. García-Pardo, T. Escribà, J. Lorenzo, M. Arnedo, D. Ruiz-Molina, R. Alibés, F. Busqué, F. Novio, Versatile Iron-Catechol-based Nanoscale Coordination Polymers with Antiretroviral Ligand Functionalization and their use as Efficient Carriers in HIV/AIDS Therapy, Biomater. Sci. 7 (2019) 178–186.

[83] For a complete review describing theranostic research since 2006 to 2013 see: E.-K. Lim, T. Kim, S. Paik, S. Haam, Y.-M. Huh, K. Lee, Nanomaterials for Theranostics: Recent Advances and Future Challenges, Chem. Rev. 115 (2015) 327–394.

[84] R. Weissleder, B. D. Ross, A. Rehemtulla, S.S. Gambhir, Molecular Imaging: Principles and Practice; People's Medical Publishing House: Shelton, CT, 2010.

[85] A. Cabrera-García, E. Checa-Chavarria, J. Pacheco-Torres, A. Bernabeu-Sanz, A. Vidal-Moya, E. Rivero-Buceta, G. Sastre, E. Fernández, P. Botella, Engineered Contrast Agents in a Single Structure for: T1-T2 Dual Magnetic Resonance Imaging. Nanoscale 10 (2018), 6349–6360.

[86] M. Rogosnitzky, S. Branch, Gadolinium-Based Contrast Agent Toxicity: A Review of Known and Proposed Mechanisms, BioMetals 29 (2016) 365–376.

[87] J. Ramalho, R. C. Semelka, M. Ramalho, R.H. Nunes, M. AlObaidy, M. Castillo, Gadolinium–Based Contrast Agent Accumulation and Toxicity: An Update, Am. J. Neuroradiol. 37 (2016) 1192–1198.

[88] N. Lee, T. Hyeon, Designed Synthesis of Uniformly Sized Iron Oxide Nanoparticles for Efficient Magnetic Resonance Imaging Contrast Agents. Chem. Soc. Rev. 41 (2012) 2575–2589.

[89] K. M. Hasebroock, N. J. Serkova, Toxicity of MRI and CT Contrast Agents, Expert Opin. Drug Metab. Toxicol. 5 (2009) 403–416.

[90] A. Z. Khawaja, D. B. Cassidy, J. Al Shakarchi, D. G. McGrogan, N. G. Inston, R. G. Jones, Revisiting the Risks of MRI with Gadolinium Based Contrast Agents-review of Literature and Guidelines, Insights Imaging 6 (2015) 553–558.

[91] K. M. Erikson, A. W. Dobson, D. C. Dorman, M. Aschner, Manganese Exposure and Induced Oxidative Stress in the Rat Brain, Sci. Total Environ. 334-335 (2004) 409–416.

[92] E. Kanal, M. F. Tweedle, Residual or Retained Gadolinium: Practical Implications for Radiologists and Our Patients, Radiology 275 (2015) 630–634.

[93] R. J. McDonald, J. S. McDonald, D. F. Kallmes, M. E. Jentoft, D. L. Murray, K. R. Thielen, E. E. Williamson, L. J. Eckel, Gadolinium Deposition after Contrast-Enhanced MR Imaging, Radiology 275 (2015) 772–782.

[94] K.M.L. Taylor, J.S. Kim, W.J. Rieter, H. An, W. Lin, W. Lin, Mesoporous Silica Nanospheres as Highly Efficient MRI Contrast Agents, J. Am. Chem. Soc. 130 (2008) 2154-2155.

[95] A.R. Chowdhuri, D. Bhattacharya, S.K. Sahu, Magnetic Nanoscale Metal Organic Frameworks for Potential Targeted Anticancer Drug Delivery, Imaging and as an MRI Contrast Agent. Dalton Trans. 45 (2016) 2963–2973.

[96] Z. He, P. Zhang, Y. Xiao, J. Li, F. Yang, Y. Liu, J. R. Zhang, J. J. Zhu, Acid–Degradable Gadolinium–Based Nanoscale Coordination Polymer: A Potential Platform for Targeted Drug Delivery and Potential Magnetic Resonance Imaging, Nano Res. 11 (2018) 929–939.

[97] H.S. Choi, P. Misra, M. G. Bawendi, J. V. Frangioni, B. Ipe, W. Liu, J. P. Zimmer, E. Tanaka, Renal Clearance of Quantum Dots, Nat. Biotechnol. 25 (2007) 1165–1170.

[98] M. Perrier, A. Gallud, A. Ayadi, S. Kennouche, C. Porredon, M. Gary–Bobo, J. Larionova, C. Goze–Bac, M. Zanca, M. Garcia, I. Basile, J. Long, J. de Lapuente, M. Borras, Y. Guaria, Investigation of Cyano-Bridged Coordination Nanoparticles Gd^{3+}/$[Fe(CN)_6]_3$–/D–Mannitol as T1-Weighted MRI Contrast Agents, Nanoscale 7 (2015) 11899–11903.

[99] J. Ma, H. Dong, H. Zhu, C.W. Li, Y. Li, D. Shi, Deposition of Gadolinium onto the Shell Structure of Micelles for Integrated Magnetic Resonance Imaging and Robust Drug Delivery Systems, J. Mater. Chem. B 4 (2016) 6094–6102.

[100] J. Qin, G. Liang, B. Feng, G. Wang, N. Wu, Y. Deng, A.A. Elzatahry, A. Alghamdi, Y. Zhao, J. Wei, Facile Synthesis of Metal-Polyphenol-Formaldehyde Coordination Polymer Colloidal Nanoparticles with Sub-50 nm for T1-Weighted Magnetic Resonance Imaging, Chin. Chem. Lett. (2020) In press.

[101] Z.P. Xu, N.D. Kurniawan, P.F. Bartlett, G.Q. Lu, Enhancement of Relaxivity Rates of Gd-DTPA Complexes by Intercalation into Layered Double Hydroxide Nanoparticles, Chem. Eur. J. 13 (2007) 2824–2830.

[102] M.A. Sieber, T. Steger-Hartmann, P. Lengsfeld, H. Pietsch, Gadolinium-Based Contrast Agents and NSF: Evidence from Animal Experience, J Magn. Reson. Imaging 30 (2009) 1268–1276.

[103] M.R. Prince, H.L. Zhang, J.C. Prowda, M.E. Grossman, D.N. Silvers, Nephrogenic Systemic Fibrosis and its Impact on Abdominal Imaging, Radiographics 29 (2009) 1565–1574.

[104] J.M. Idee, M. Port, A. Dencausse, E. Lancelot, C. Corot, Involvement of gadolinium chelates in the mechanism of nephrogenic systemic fibrosis: an update, Radiol. Clin. North Am. 47 (2009) 855-869.

[105] P. Caravan, J.J. Ellison, T.J. McMurry, R.B. Lauffer, Gadolinium(III) Chelates as MRI Contrast Agents: Structure, Dynamics, and Applications, Chem. Rev. 99 (1999) 2293–2352.

[106] D. Liu, C. He, C. Poon, W. Lin, Theranostic Nanoscale Coordination Polymers for Magnetic Resonance Imaging and Bisphosphonate Delivery, J. Mater. Chem. B 2 (2014) 8249–8255.

[107] Y. Yang, J. Liu, C. Liang, L. Feng, T. Fu, Z. Dong, Y. Chao, Y. Li, G. Lu, M. Chen, Z. Liu, Nanoscale Metal-Organic Particles with Rapid Clearance for Magnetic Resonance Imaging-Guided Photothermal Therapy, ACS Nano 10 (2016) 2774–2781.

[108] J. Zhao, Y. Yang, X. Han, C. Liang, J. Liu, X. Song, Z. Ge, Z. Liu, Redox-Sensitive Nanoscale Coordination Polymers for Drug Delivery and Cancer Theranostics, ACS Appl. Mater. Interfaces 9 (2017) 23555–23563.

[109] H. Zhang, K. Liu, S. Li, X. Xin, S. Yuan, G. Ma, X. Yan, Self-Assembled Minimalist Multifunctional Theranostic Nanoplatform for Magnetic Resonance Imaging-Guided Tumor Photodynamic Therapy, ACS Nano 12 (2018) 8266–8276.

[110] H.-W. Shin, H. Sohn, Y.-H. Jeong, S.-M. Lee, Construction of Paramagnetic Manganese-Chelated Polymeric Nanoparticles Using Pyrene-End-Modified Double-Hydrophilic Block Copolymers for Enhanced Magnetic Resonance Relaxivity: A Comparative Study with Cisplatin Pharmacophore, Langmuir 35 (2019) 6421–6428.

[111] Y. Wu, L. Xu, J. Qian, L. Shi, Y. Su, Y. Wang, D. Li, X. Zhu, Methotrexate-Mn^{2+} Based Nanoscale Coordination Polymers as a Theranostic Nanoplatform for MRI Guided Chemotherapy, Biomater. Sci. 8 (2020) 712–719.

[112] J. Huang, L. Bu, J. Xie, K. Chen, Z. Cheng, X. Li, Effects of Nanoparticle Size on Cellular Uptake and Liver MRI with Polyvinylpyrrolidone-Coated Iron Oxide Nanoparticles, ACS Nano 4 (2010) 7151–7160.

[113] J. Xie, S. Lee, X. Chen, Nanoparticle-Based Theranostic Agents, Adv. Drug Deliv. Rev. 62 (2010) 1064–1079.

[114] J. Xie, K. Chen, J. Huang, S. Lee, J. Wang, J. Gao, PET/NIRF/MRI Triple Functional Iron Oxide Nanoparticle, Biomaterials 31 (2010) 3016–3022.

[115] T. Kim, E. Momin, J. Choi, K. Yuan, H. Zaidi, J. Kim, Mesoporous Silica-Coated Hollow Manganese Oxide Nanoparticles as Positive T1 Contrast Agents for Labeling and MRI Tracking of Adipose-Derived Mesenchymal Stem Cell, J. Am. Chem. Soc. 133 (2011) 2955–2961.

[116] X. Mu, C. Yan, Q. Tian, J. Lin, S. Yang, BSA-Assisted Synthesis of Ultrasmall Gallic Acid-Fe(III) Coordination Polymer Nanoparticles for Cancer Theranostics, Int. J. Nanomedicine 12 (2017) 7207–7223.

[117] L. Xing, H. Zheng, Y. Cao, S. Che, Coordination Polymer Coated Mesoporous Silica Nanoparticles for pH-Responsive Drug Release, Adv. Mater. 24 (2012) 6433–6437.

[118] H. Zheng, L. Xing, Y. Cao, S. Che, Coordination Bonding Based pH-Responsive Drug Delivery Systems, Coord. Chem. Rev. 257 (2013) 1933–1944.

[119] C. Zhang, J. Li, C. Yang, S. Gong, H. Jiang, M. Sun, C Qian, A pH-Sensitive Coordination Polymer Network-Based Nanoplatform for Magnetic Resonance Imaging-Guided Cancer Chemo-Photothermal Synergistic Therapy, Nanomed. Nanotechnol. 23 (2020) 102071.

[120] K. Xin, M. Li, D. Lu, X. Meng, J. Deng, D. Kong, D. Ding, Z. Wang, Y. Zhao, Bioinspired Coordination Micelles Integrating High Stability, Triggered Cargo Release, and Magnetic Resonance Imaging, ACS Appl. Mater. Interfaces 9 (2017) 80–91.

[121] J. Qin, G. Liang, Y. Feng, B. Feng, G. Wang, N. Wu, Y. Zhao, J. Wei, Synthesis of Gadolinium/Iron–Bimetal-Phenolic Coordination Polymer Nanoparticles for Theranostic Applications, Nanoscale, 12 (2020) 6096-6103.

[122] H. Yang, C. Qin, C. Yu, Y. Lu, H. Zhang, F. Xue, D. Wu, Z. Zhou, S. Yang, RGD-Conjugated Nanoscale Coordination Polymers for Targeted T1- and T2-Weighted Magnetic Resonance Imaging of Tumors in Vivo, Adv. Funct. Mater. 24 (2013) 1738–1747.

[123] Y. Chen, K. Ai, J. Liu, X. Ren, C. Jiang, L. Lu, Polydopamine-Based Coordination Nanocomplex for T1/T2 Dual Mode Magnetic Resonance Imaging-Guided Chemo-Photothermal Synergistic Therapy, Biomaterials 77 (2016) 198–206.

[124] M. Borges, S. Yu, A. Laromaine, A. Roig, S. Suárez-García, J. Lorenzo, D. Ruiz-Molina, F. Novio, Dual T1/T2 MRI Contrast Agent Based on Hybrid SPION@Coordination Polymer Nanoparticles, RSC Adv. 5 (2015) 86779–86783.

[125] S. Suárez–García, N. Arias-Ramos, C. Frias, A. P. Candiota, C. Arús, J. Lorenzo, D. Ruiz-Molina, F. Novio, Dual T1/T2 Nanoscale Coordination Polymers as Novel Contrast Agents for MRI: A Preclinical Study for Brain Tumor, ACS Appl. Mater. Interfaces 10 (2018) 38819–38832.

[126] U. Speck in Handbook of Experimental Pharmacology,Vol. 185 (Eds.: W. Semmler, M. Schwaiger), Springer, Berlin, 2008, pp. 167–175.

[127] K.E. deKrafft, Z. Xie, G. Cao, S. Tran, L. Ma, O.Z. Zhou, W. Lin, Nanoscale Coordination Polymers as Potential Contrast Agents for Computed Tomography, Angew. Chem. Int. Ed. 48 (2009) 9901–9904.

[128] J. Liu, G. Yang, W. Zhu, Z. Dong, Y. Yang, Y. Chao, Z. Liu, Light-Controlled Drug Release from Singlet-Oxygen Sensitive Nanoscale Coordination Polymers Enabling Cancer Combination Therapy, Biomaterials 146 (2017) 40–48.

[129] A.P. Alivisatos, Semiconductor Clusters, Nanocrystals, and Quantum Dots, Science 271 (1996) 933–937.

[130] J.K. Jaiswal, H. Mattoussi, J.M. Mauro, S.M. Simon, Long-Term Multiple Color Imaging of Live Cells Using Quantum Dot Bioconjugates, Nat. Biotechnol. 21 (2002) 47–51.

[131] M.A. El-Sayed, Small Is Different: Shape-, Size-, and Composition-Dependent Properties of Some Colloidal Semiconductor Nanocrystals, Acc. Chem. Res. 37 (2004) 326–333.

[132] N.L. Rosi, C.A. Mirkin, Nanostructures in Biodiagnostics, Chem. Rev. 105 (2005) 1547–1562.

[133] C. Burda, X.B. Chen, R. Narayana, M.A. El-Sayed, Chemistry and Properties of Nanocrystals of Different Shapes, Chem. Rev. 105 (2005) 1025–1102.

[134] Z. Kang, Y. Liu, C.H.A. Tsang, D.D.D. Ma, X. Fan, N.-B. Wong, S.-T. Lee, Water-Soluble Silicon Quantum Dots with Wavelength-Tunable Photoluminescence, Adv. Mater. 21 (2009) 661–664.

[135] B. Dubertret, P. Skourides, D.J. Norris, V. Noireaux, A.H. Brivanlou, A. Libchaber, In Vivo Imaging of Quantum Dots Encapsulated in Phospholipid Micelles, Science 298 (2002) 1759–1762.

[136] L. Zhang, X. Qian, L. Liu, Z. Shi, Y. Li, S. Wang, H. Liu, Y. Lia, Water-Dispersed Quantum Dots of Coordination Polymers with Strong Photoluminescence, Chem. Commun. 48 (2012) 6166–6168.

[137] S.L. Zhong, R. Xu, L.F. Zhang, W.G. Qu, G.Q. Gao, X.L. Wub, A.W. Xu, Terbium-Based Infinite Coordination Polymer Hollow Microspheres: Preparation and White-Light Emission, J. Mater. Chem. 21 (2011) 16574–16580.

[138] C. Aimé, R. Nishiyabu, R. Gondo, N. Kimizuka, Switching on Luminescence in Nucleotide/Lanthanide Coordination Nanoparticles via Synergistic Interactions with a Cofactor Ligand, Chem. Eur. J. 16 (2010) 3604–3607.

[139] W.Liu, Y. Wang, Y.H. Li, S.J. Cai, X. B. Yin, X.W. He, Y.K. Zhang, Fluorescent Imaging-Guided Chemotherapy-and-Photodynamic Dual Therapy with Nanoscale Porphyrin Metal-Organic Framework, Small 13 (2017) 1–8.

[140] D. Liu, R.C. Huxford, W. Lin, Phosphorescent Nanoscale Coordination Polymers as Contrast Agents for Optical Imaging, Angew. Chem. Int. Ed. 50 (2011) 3696–3700.

[141] Q. Ban, J. Du, W. Sun, J. Chen, S. Wu, J. Kong, Intramolecular Copper-Containing Hyperbranched Polytriazole Assemblies for Label-free Cellular Bioimaging and Redox-Triggered Copper Complex Delivery, Macromol. Rapid Commun. 39 (2018) 1800171.

[142] J. G. Heck, J. Napp, S. Simonato, J. Möllmer, M. Lange, H.M.; Reichardt, R. Staudt, F. Alves, C. Feldmann, Multifunctional Phosphate-Based Inorganic-Organic Hybrid Nanoparticles, J. Am. Chem. Soc. 137 (2015) 7329−7336.

[143] C. Sahub, G. Tumcharern, P. Chirawatkul, V. Ruangpornvisuti, S. Ekgasit, S. Wanichweacharungruang, T. Tuntulani, T. Palaga, B. Tomapatanaget, Self-Assembly of Gd^{3+} /SDS/HEPES Complex and Curcumin Entrapment for Enhanced Stability, Fluorescence Image in Cellular System, Colloids Surf. B 156 (2017) 254–261.

[144] D. Liu, C. Poon, K. Lu, C. He, W. Lin, Self–Assembled Nanoscale Coordination Polymers with Trigger Release Properties for Effective Anticancer Therapy, Nat. Commun. 5 (2014) 4182.

[145] C. Poon, C. He, D. Liu, K. Lu, W. Lin, Self–Assembled Nanoscale Coordination Polymers Carrying Oxaliplatin and Gemcitabine for Synergic Cancer, J. Control, Release 201 (2015) 90–99.

[146] Y. Peng, P. Liu, Y. Meng, S. Hu, J. Ding, W. Zhou, Nanoscale Copper(II)−Diethyldithiocarbamate Coordination Polymer as a Drug Self-Delivery System for Highly Robust and Specific Cancer Therapy, Mol. Pharmaceutics 17 (2020) 2864−2873.

[147] F. Nador, K. Wnuk, J. García-Pardo, J.; Lorenzo, R. Solórzano, D. Ruiz-Molina, F. Novio, Dual-Fluorescent Nanoscale Coordination Polymers via a Mixed-Ligand Synthetic Strategy and Their Use for Multichannel Imaging, ChemNanoMat 4 (2018) 183–193.

[148] M. D. Farwell, D. A. Pryma, D. A. Mankoff, PET/CT Imaging in Cancer, Current Applications and Future Directions, Cancer 120 (2014) 3433–3445.

[149] L. Zhu, K. Ploessl, H. F. Kung, PET/SPECT Imaging Agents for Neurodegenerative Diseases, Chem. Soc. Rev. 43 (2014) 6683–6691.

[150] C. Wu, F. Li, G. Niu, X Chen, PET Imaging of Inflammation Biomarkers, Theranostics 3 (2013) 448–466.

[151] D. Ulmert, L. Solnes, D.L.J. Thorek, Contemporary Approaches for Imaging Skeletal Metastasis, Bone Res. 3 (2015) 15024.

[152] H. Hong, F. Chen, Y. Zhang, W. Cai, New Radiotracers for Imaging of Vascular Targets in Angiogenesis-Related Diseases, Adv. Drug Deliv. Rev. 76 (2014) 2–20.

[153] C.S. Cutler, H.M. Hennkens, N. Sisay, S. Huclier–Markai, S.S. Jurisson, Radiometals for Combined Imaging and Therapy, Chem. Rev. 113 (2013) 858–883.

[154] M. S. Oh, S. H. Jung, S. H. Choi, Synthesis and Characterization of Coordination Polymer Nanoparticles as Radioisotope Tracers, Appl. Radiat. Isot. 85 (2014) 19–22.

[155] M. S. Oh, S. H. Jung, S. H. Choi, Preparation of Radioisotope Nanoparticles Constructed with Au-Ligand Framework by Self-Assembly Process for Radiotracer, J. Radioanal. Nucl. Chem. 302 (2014) 1151–1158.

[156] S. Shen, D. Jiang, L. Cheng, Y. Chao, K. Nie, Z. Dong, C.J. Kutyreff, J.W. Engle, P. Huang, W. Cai, Z. Liu, Renal-Clearable Ultrasmall Coordination Polymer Nanodots for Chelator-Free ^{64}Cu–Labeling and Imaging-Guided Enhanced Radiotherapy of Cancer, ACS Nano 11 (2017) 9103–9111.

[157] H. D. Lu, L. Z. Wang, B. K. Wilson, S. A. McManus, J. Jumai'An, P. K. Padakanti, A. Alavi, R. H. Mach, R. K. Prud'Homme, Copper Loading of Preformed Nanoparticles for PET-Imaging Applications, ACS Appl. Mater. Interfaces 10 (2018) 3191–3199.

[158] Y. Yang, W. Zhu, L. Feng, Y. Chao, Y. Yi, Z. Dong, K. Yang, W. Tan, Z. Liu, M. Chen, G-Quadruplex–Based Nanoscale Coordination Polymers to Modulate Tumor Hypoxia and Achieve

Nuclear-Targeted Drug Delivery for Enhanced Photodynamic Therapy, Nano Lett. 18 (2018) 6867−6875.

[159] Y. Chao, C. Liang, Y. Yang, G. Wang, D. Maiti, L. Tian, F. Wang, W. Pan, S. Wu, Y. Yang, Z. Liu, Highly Effective Radioisotope Cancer Therapy with a Non-Therapeutic Isotope Delivered and Sensitized by Nanoscale Coordination Polymers, ACS Nano 12 (2018) 7519−7528.

[160] L.V. Wang, S. Hu, Photoacoustic Tomography: In Vivo Imaging from Organelles to Organs, Science 335 (2012) 1458e1462.

[161] J. Weber, P.C. Beard, S.E. Bohndiek, Contrast agents for molecular photo-acoustic imaging, Nat. Methods 13 (2016) 639e650.

[162] K.A. Homan, M. Souza, R. Truby, G.P. Luke, C. Green, E. Vreeland, S. Emelianov, Silver Nanoplate Contrast Agents for In Vivo Molecular Photoacoustic Imaging, ACS Nano 6 (2012) 641-650.

[163] J. Zhang, X. Zhen, P.K. Upputuri, M. Pramanik, P. Chen, K. Pu, Activatable Photoacoustic Nanoprobes for In Vivo Ratiometric Imaging of Peroxynitrite, Adv. Mater. 29 (2017) 1604764.

[164] X. Wang, Y. Pang, G. Ku, X. Xie, G. Stoica, L.V. Wang, Non Invasive Laser-Induced Photoacoustic Tomography for Structural and Functional In Vivo Imaging of the Brain, Nat. Biotechnol. 21 (2003) 803-806.

[165] M.F. Kircher, A. De La Zerda, J.V. Jokerst, C.L. Zavaleta, P.J. Kempen, E. Mittra, K. Pitter, R. Huang, C. Campos, F. Habte, R. Sinclair, C.W. Brennan, I.K. Mellinghoff, E.C. Holland, S.S. Gambhir, A Brain Tumor Molecular Imaging Strategy Using a New Triple-Modality MRI-Photoacoustic-Raman Nanoparticle, Nat. Med. 18 (2012) 829-834.

[166] D. Pan, M. Pramanik, A. Senpan, J.S. Allen, H. Zhang, S.A. Wickline, L.V. Wang, G.M. Lanza, Molecular Photoacoustic Imaging of Angiogenesis with Integrin-Targeted Gold Nano Beacons, FASEB J 25 (2011) 875-882.

[167] J. Laufer, P. Johnson, E. Zhang, B. Treeby, B. Cox, B. Pedley, P. Beard, In Vivo Preclinical Photoacoustic Imaging of Tumor Vasculature Development and Therapy, J. Biomed. Opt. 17 (2012) 0560161-0560168.

[168] B. Wang, Q. Zhao, N.M. Barkey, D.L. Morse, H. Jiang, Photoacoustic Tomography and Fluorescence Molecular Tomography: A Comparative Study Based on Indocyanine Green, Med. Phys. 39 (2012) 2512-2517.

[169] Y. Liu, L. Teng, H.-W. Liu, C. Xu, H. Guo, L. Yuan, X.-B. Zhang, W. Tan, Recent Advances in Organic-Dye-Based Photoacoustic Probes for Biosensing and Bioimaging, Sci. China Chem., 62 (2019) 1275–1285.

[170] L. Li, A. A. Shemetov, M. Baloban, P. Hu, L. Zhu, D. M. Shcherbakova, R. Zhang, J. Shi, J. Yao, L. V. Wang, V. V. Verkhusha, Small Near-Infrared Photochromic Protein for Photoacoustic Multi-Contrast Imaging and Detection of Protein Interactions In Vivo, Nat. Commun. 9 (2018) 2734.

[171] S. Han, R. Bouchard, K. V. Sokolov, Molecular Photoacoustic Imaging with Ultra-Small Gold Nanoparticles, Biomed. Opt. Express. 10 (2019) 3472–3483.

[172] H. Gong, R. Peng, Z. Liu, Carbon Nanotubes for Biomedical Imaging: The Recent Advances, Adv. Drug Deliv. Rev. 65 (2013) 1951-1963.

[173] L. Fusco, A. Gazzi, G. Peng, Y. Shin, S. Vranic, D. Bedognetti, F. Vitale, A. Yilmazer, X. Feng, B. Fadeel, C. Casiraghi, L. G. Delogu, Graphene and other 2D Materials: A Multidisciplinary Analysis to Uncover the Hidden Potential as Cancer Theranostics, Theranostics 10 (2020) 5435-5488.

[174] M. González-Béjar, L. Francés-Soriano, J. Pérez-Prieto, Upconversion Nanoparticles for Bioimaging and Regenerative Medicine, Front. Bioeng. Biotechnol. 4 (2016) 47.

[175] K. Pu, A.J. Shuhendler, J.V. Jokerst, J. Mei, S.S. Gambhir, Z. Bao, J. Rao, Semiconducting Polymer Nanoparticles as Photoacoustic Molecular Imaging Probes in Living Mice, Nat. Nanotech. 9 (2014) 233–239.

[176] C. Xie, X. Zhen, Y. Lyu, K. Pu, Nanoparticle Regrowth Enhances Photoacoustic Signals of Semiconducting Macromolecular Probe for In Vivo Imaging, Adv. Mat. 29 (2017) 1703693.

[177] X. Zhen, X. Feng, C. Xie, Y. Zheng, K. Pu, Surface engineering of semiconducting polymer nanoparticles for amplified photoacoustic imaging, Biomaterials 127 (2017) 97-106.

[178] Y. Wang, F. Liu, N. Yan, S. Sheng, C. Xu, H. Tian, X. Chen, Exploration of Fe^{III}-Phenol Complexes Therapy and Photoacoustic Imaging, ACS Biomater. Sci. Eng. 5 (2019) 47003–4707.

[179] Z. Zhou, D. Li, H. Yang, Y. Zhu, S. Synthesis of d-f Coordination Polymernanoparticles and their Application in Phosphorescence and Magnetic Resonance Imaging, Dalton Trans. 40 (2011) 11941–11944.

[180] Y. Lu, F. Xue, H. Yang, M. Shi, Y. Yan, L. Qin, Z. Zhou, S. Yang, Phosphorescent Coordination Polymer Nanoparticles as a Three-in-One Platform for Optical Imaging, T1–Weighted Magnetic Resonance Imaging, and Photodynamic Therapy, J. Phys. Chem. C 119 (2015) 573–579.

[181] Y. M. Wang, W. Liu, X. B. Yin, Multifunctional Mixed–Metal Nanoscale Coordination Polymers for Triple–Modality Imaging–Guided Photodynamic Therapy, Chem. Sci. 8 (2017) 3891–3897.

[182] J. Cui, G. Zhang, L. Xin, P. Yun, Y. Yan, F. Su, Functional Nanoscale Metal-Organic Particles Synthesized from a New Vinylimidazole-Based Polymeric Ligand and Dysprosium Ions, J. Mater. Chem. C 6 (2017) 280–289.

[183] Y. M. Wang, W. Liu, X. B. Yin, Self-Limiting Growth Nanoscale Coordination Polymers for Fluorescence and Magnetic Resonance Dual-Modality Imaging, Adv. Funct. Mater. 26 (2016) 8463–8470.

[184] W. Sun, L. Luo, Y. Feng, Y. Qiu, C. Shi, S. Meng, X. Chen, H. Chen, Gadolinium–Rose Bengal Coordination Polymer Nanodots for MR-/Fluorescence-Image-Guided Radiation and Photodynamic Therapy, Adv. Mater. 32 (2020) 2000377.

[185] Q. An, J. Liu, M. Yu, J. Wan, D. Li, C. Wang, C. Chen, J. Guo, Multifunctional Magnetic Gd^{3+}-Based Coordination Polymer Nanoparticles: Combination of Magnetic Resonance and Multispectral Optoacoustic Detections for Tumor-Targeted Imaging in Vivo, Small 11 (2015) 5675–5686.

[186] D. Hu, C. Liu, L. Song, H. Cui, G. Gao, P. Liu, Z. Sheng, L. Cai, Indocyanine Green–Loaded Polydopamine–Iron Ions Coordination Nanoparticles for Photoacoustic/Magnetic Resonance Dual–Modal Imaging-Guided Cancer Photothermal Therapy, Nanoscale 8 (2016) 17150–17158.

[187] Y. Yang, W. Zhu, Z. Dong, Y. Chao, L. Xu, M. Chen, Z. Liu, Z. 1D Coordination Polymer Nanofibers for Low-Temperature Photothermal Therapy, Adv. Mater. 29 (2017) 1703588.

[188] Y. Yang, Y. Chao, J. Liu, Z. Dong, W. He, R. Zhang, K. Yang, M. Chen, Z. Liu, Core-Shell and Co-Doped Nanoscale Metal-Organic Particles (NMOPs) Obtained via Post-Synthesis Cation Exchange for Multimodal Imaging and Synergistic Thermo-Radiotherapy, NPG Asia Mater. 9 (2017) e344–11.

[189] Q. Tian, Y. Cai, N. Li, Q. Liu, B. Gu, Z.-G. Chen, S. Song, Ellagic Acid–Fe Nanoscale Coordination Polymer with Higher Longitudinal Relaxivity for Dual-ModalityT1-Weighted Magnetic Resonance and Photoacoustic Tumor Imaging, Nanomed. Nanotechnol. 28 (2020) 102219.

[190] Q. Jin, W. Zhu, D. Jiang, R. Zhang, C.J. Kutyreff, J. W. Engle, P. Huang, W. Cai, Z. Liu, L. Cheng, Ultra-Small Iron-Gallic Acid Coordination Polymer Nanoparticles for Chelator-Free Labeling of ^{64}Cu and Multimodal Imaging-Guided Photothermal Therapy, Nanoscale 9 (2017) 12609–12617.

[191] C. Chu, E. Ren, Y. Zhang, J. Yu, H. Lin, X. Pang, Y. Zhang, H. Liu, Z. Qin, Y. Cheng, X. Wang, W. Li, X. Kong, X. Chen, G. Liu, Zinc(II)–Dipicolylamine Coordination Nanotheranostics: Toward Synergistic Nanomedicine by Combined Photo/Gene Therapy, Angew. Chem. Int. Ed. 58 (2019) 269–272.

[192] J. Huang, C. Xie, X. Zhang, Y. Jiang. J. Li, Q. Fan, K. Pu, Renal-clearable Molecular Semiconductor for Second Near-Infrared Fluorescence Imaging of Kidney Dysfunction, Angew. Chem. Inter. Ed., 58 (2019) 15120-15127.

[193] Y. Jiang, P. K. Upputuri, C. Xie, Z. Zeng, A. Sharma, X. Zhen, J. Li, J. Huang, M. Pramanik, K. Pu, Metabolizable Semiconducting Polymer Nanoparticles for Second Near-Infrared Photoacoustic Imaging, Adv. Mater. 31 (2019) 1808166.

[194] Y. Jiang, J. Huang, X. Zhen, Z. Zeng, J. Li, C. Xie, Q. Miao, J. Chen, P. Chen, K. Pu, A Generic Approach Towards Afterglow Luminescent Nanoparticles for Ultrasensitive In Vivo Imaging, Nat. Commun. 10 (2019) 2064.

[195] Q. Miao, C. Xie, X. Zhen, Y. Lyu, H. Duan, X. Liu, J. V. Jokerst, K. Pu, Molecular Afterglow Imaging with Bright, Biodegradable Polymer Nanoparticles, Nat. Biotech. 35 (2017) 1102-1110.

[196] J. Huang, J. Li, Y. Lyu, Q. Miao, K. Pu, Molecular Optical Imaging Probes for Early Diagnosis of Drug-Induced Acute Kidney Injury, Nat. Mater. 18 (2019) 1133.

[197] P. Cheng, Q. Miao, J. Li, J. Huang, C. Xie, K. Pu, Unimolecular Chemo-Fluoro-Luminescent Reporter for Crosstalk-Free Duplex Imaging of Hepatotoxicity, J. Am. Chem. Soc. 141 (2019) 10581-10584.

[198] M. Rohrer , H. Bauer , J. Mintorovitch , M. Requardt, H.-J. Weinmann, Comparison of Magnetic Properties of MRI Contrast Media Solutions at Different Magnetic Field Strengths, Invest. Radiol. 40 (2005) 715-724.

[199] L. Li, W. Jiang, K. Luo, H. Song, F. Lang, Y. Wu, Z. Gu, Superparamagnetic Iron Oxide Nanoparticles as MRI Contrast Agents for Non-invasive Stem Cell Labeling and Tracking, Theranostics 3 (2013) 595-615.